Daytime-only-mean data ~~can enhance~~ enhances understanding of land-atmosphere coupling

Zun Yin[1], Kirsten L. Findell[2], Paul Dirmeyer[3], Elena Shevliakova[2], Sergey Malyshev[2], Khaled Ghannam[1], Nina Raoult[4], and Zhihong Tan[1]

[1]Program in Atmospheric and Oceanic Sciences, Princeton University, Princeton, 08540, New Jersey, USA
[2]Geophysical Fluid Dynamics Laboratory, NOAA, Princeton, 08540, New Jersey, USA
[3]Center for Ocean-Land-Atmosphere Studies, George Mason University, Fairfax, 22030, Virginia, USA
[4]Laboratoire des Sciences du Climat et de l'Environnement, IPSL, CNRS-CEA-UVSQ, Gif-sur-Yvette, 91191, Essonne, France

Correspondence: Zun Yin (zyin@princeton.edu)

Abstract. Land-atmosphere (L-A) interactions encompass the co-evolution of the land surface and overlying planetary boundary layer, primarily during daylight hours. However, many studies have been conducted using monthly or entire-day-mean time series due to the lack of sub-daily data. It ~~has been~~ is unclear whether the inclusion of nighttime data alters the assessment of L-A coupling or obscures L-A interactive processes. To address this question, we generate monthly (M), entire-day-mean (E), and daytime-only-mean (D) data based on the ERA5 (5th European Centre for Medium-Range Weather Forecasts reanalysis) product, and evaluate the strength of L-A coupling through two-legged metrics, which partition the impact of the land states on surface fluxes (the land leg) from the impact of surface fluxes on the atmospheric states (the atmospheric leg). Here we show that the spatial patterns of strong L-A coupling regions among the M-, D- and E-based diagnoses can differ by ~~as much as 84.8~~more than 80%. The signal loss from E- to M-based diagnoses is determined by the memory of local L-A states. The differences between E- and D-based diagnoses can be driven by physical mechanisms or the averaging algorithms. To improve understanding of L-A interactions, we call attention to the urgent need for more high-frequency data from both simulations and observations for relevant diagnoses. Regarding model outputs, two approaches are proposed to resolve the storage dilemma for high-frequency data: (1) integration of L-A metrics within Earth System Models, and (2) producing alternative daily datasets based on different averaging algorithms.

1 Introduction

Numerous studies have demonstrated the importance of land-atmosphere (L-A) interactions to the earth system (Findell et al., 2011; Hu et al., 2021; Klein and Taylor, 2020; Laguë et al., 2019; Taylor et al., 2012). Manifested by the mass and energy exchanges between the land surface and the planetary boundary layer (PBL), L-A interactions ~~determine~~ influence the evolution of ~~the convective system~~ convective systems (Hu et al., 2021; Klein and Taylor, 2020) as well as the occurrence of convective rainfall (Taylor et al., 2012). From a climatic perspective, ~~the~~ coupling processes between the land and the atmosphere can accelerate the frequency and intensity of extreme events (Dirmeyer et al., 2021; Miralles et al., 2019; Schumacher et al., 2019; Zhou et al., 2021) and the shift of climate regimes (Berg et al., 2017; Findell et al., 2019) under global warming. To better understand L-A interactions, a suite of metrics has been proposed for characterizing specific physical processes across broad spatial and temporal scales (Santanello et al., 2018). These metrics can reveal essential behaviors of L-A interactions and enhance our understanding of the coupling mechanisms (e.g., (Chen and Dirmeyer, 2017; Findell et al., 2011; Hu et al., 2021; Jach et al., 2022) Chen and Dirmeyer (2017); Findell et al. (2011); Hu et al. (2021); Jach et al. (2022)). Additionally, they provide a benchmark to evaluate the performance of earth system models in simulating L-A coupling processes (e.g., (Dirmeyer et al., 2018; Ferguson et al., 2012 Dirmeyer et al. (2018); Ferguson et al. (2012); Koster et al. (2006); Santanello et al. (2009)).

However, L-A interactions alone are not always the primary determinant in the climate system (Koster et al., 2004). To reveal hotspots where and when L-A interactions play an important role, two criteria have been proposed: 1) the state of the atmosphere must be highly responsive to variations in land properties, and 2) there must be physically meaningful variability in those land properties over time (Dirmeyer, 2011; Guo et al., 2006; Koster et al., 2004). Dirmeyer (2011) proposed a metric (M) to characterize both features as

$$M = \frac{\mathrm{d}b}{\mathrm{d}a} \cdot \sigma_a = \rho(a,b)\sigma_b. \tag{1}$$

The M contains two components to estimate the coupling strength between variables a, presumed to be the driver, and b, the response. The coupling is significant only when b is sensitive to a (high $\mathrm{d}b/\mathrm{d}a$) and the variation of a (standard deviation of a, σ_a) is large. The formula is equivalent to the correlation coefficient between a and b (i.e., $\rho(a,b)$) multiplied by σ_b. The advantage of this metric is its vast suitability in characterizing coupling mechanisms across different scales (Chen and Dirmeyer, 2017; Guillod et al., 2014; Findell et al., 2011; Hu et al., 2021; Lorenz et al., 2015) (Chen and Dirmeyer, 2017; Guil regardless of specific variables. In terms of L-A interactions, Dirmeyer et al. (2014) divided the coupling linkage into two steps: a land leg capturing the coupling between the land surface state (typically characterized by soil moisture) and surface fluxes of heat, moisture, or momentum, called the land leg, and and an atmospheric leg capturing the coupling between the surface fluxes and the atmosphere states , called the atmospheric leg (see Sect. 2.2).

The two-legged metrics (TLMs) mainly focus on relevant processes during the daytime processes operating in response to daytime solar heating. However, data covering the same time window daylight hours is rare in available datasets. Consequently, most TLM research has been based on time series of monthly or 24-hour average quantities (e.g., Dirmeyer et al. (2014); Hu et al. (2021); Lorenz et al. (2015)). Although these studies enhance our understanding of the patterns and seasonality of L-A coupling, it has yet to be shown whether the monthly- and entire-day-based inputs are able to accurately capture areas with strong daytime land-atmosphere couplingaccurately. In other words, are there significant differences among monthly-, entire-day-, and daytime-only-based L-A coupling diagnoses? If so, are the differences exclusively due to the averaging process, or are there other L-A coupling mechanisms that may mislead the diagnoses of daytime L-A coupling?

In this study, the $0.25°$ spatial resolution ERA5 (the fifth ECMWF ReAnalysisreanalysis, (Hersbach et al., 2018)) is employed as the test bed to address these research questions. Three time series derived from ERA5 outputs, monthly-means (M), entire-day-means (E), and daytime-only-means (D), are utilized to calculate two-legged metrics (TLMs) to evaluate L-A coupling strength. We investigate the spatial pattern differences among M-, E-, and D-based diagnoses. Primary contributors to the pattern mismatch are revealed, associated mechanisms are demonstrated, and implications are discussed.

2 Methods

2.1 ERA5 data

The ERA5 reanalysis provides 0.25°-hourly ~~data determined through assimilation of~~ modeling estimates assimilated with historical observations (e.g., soil moisture, 10-m wind, 2-m humidity, and temperature (Hersbach et al., 2020)). We collected ERA5 output over land (land-ice included) every other hour from 1:00 UTC (Coordinated Universal Time) 01-Jan-2011 until 23:00 UTC 31-Dec-2020 over [180°W–180°E]×[65°S–80°N]. To be consistent with other daily ~~data~~datasets, the entire-day-mean values (E) are obtained by averaging time steps within each day based on the UTC. For the daytime-only-mean (D), the globe is divided into twenty-four time zones and the time is converted from UTC to LST (Local Solar Time). The time steps between 8am and 6pm LST are averaged to generate D values. The monthly mean (M) is a monthly average of E. To meet the minimum length requirement (Findell et al., 2015) for monthly TLMs estimations, we collected forty years of M data from 1981 through 2020. ~~There are two chains in the L-A coupling process. One is~~

There are multiple ways of describing the linkages between the land, surface fluxes, and the atmosphere that the TLM are meant to capture. For instance, the land leg can be structured to investigate how the land affects convective precipitation via the latent heat flux~~. Another is~~, or how the land influences the growth of the ~~Planetary Boundary Layer~~ planetary boundary layer (PBL) through the sensible heat flux. As it is difficult to distinguish L-A triggered convective precipitation, we select the latter in this study~~including~~, using surface soil moisture from the 0–7 cm soil layer (θ [m^3.m^{-3}]) and sensible heat flux (H [W.m^{-2}]) ~~. Moreover, to implement ERA5 validation~~ to characterize the land leg. Additionally, to enable validation of ERA5 data with ground-based observations (i.e., FLUXNET, validation results are not shown) that ~~lacks observed PBL height~~lack observed PBL heights, we select the pressure at the lifting condensation level (P_{lcl} [Pa]) to represent the atmospheric state, specifically that of the PBL~~, which~~. P_{lcl} can be estimated from three regular ground measurements: the surface pressure (P [Pa]), 2-m temperature (T_{2m} [K]), and 2-m dew-point temperature (D_{2m} [K]) (Georgakakos and Bras, 1984), as:

$$P_{\mathrm{lcl}} = P - P\left(\frac{T_{\mathrm{2m}} - D_{\mathrm{2m}}}{223.15} + 1\right)^{-3.5}. \quad (2)$$

~~P_{lcl} Pais the pressure at LCL.~~ The three time series are grouped by season. Both long-term trends and seasonality are removed to prevent them from obscuring the signal and altering the diagnoses, following Dirmeyer et al. (2012).

2.2 Two-legged metrics

The two-legged metrics (TLMs) contain a land leg and an atmospheric leg to evaluate the two coupling links in the L-A interaction chain (Dirmeyer et al., 2014; Santanello et al., 2018). If θ, H, and P_{lcl} are utilized to represent the states of the land, the surface flux, and the atmosphere, the L-A coupling metrics (Eq. 1) can be formulated to assess the two-stepped coupling processes as:

$$\begin{aligned}
\mathcal{L} &= \frac{\mathrm{d}H}{\mathrm{d}\theta}\sigma_\theta = \rho(\theta, H)\cdot\sigma_H, \\
\mathcal{A} &= \frac{\mathrm{d}P_{\mathrm{lcl}}}{\mathrm{d}H}\sigma_H = \rho(H, P_{\mathrm{lcl}})\cdot\sigma_{P_{\mathrm{lcl}}}, \\
\mathcal{T} &= \frac{\mathrm{d}H}{\mathrm{d}\theta}\frac{\mathrm{d}P_{\mathrm{lcl}}}{\mathrm{d}H}\sigma_\theta = \rho(\theta, H)\rho(H, P_{\mathrm{lcl}})\cdot\sigma_{P_{\mathrm{lcl}}}.
\end{aligned} \tag{3}$$

$\mathcal{L}$, $\mathcal{A}$, and $\mathcal{T}$ indicate the land, the atmospheric, and the total legs, respectively. By applying to Eq. 3 to the M, E, and D time series, we can get different versions of TLMs, denoted by $\mathrm{TLM_M}$, $\mathrm{TLM_E}$, and $\mathrm{TLM_D}$, respectively. For a specific variable and leg, we use M, E, and D as subscripts to distinguish them (e.g., $\mathcal{L}_\mathrm{M}$, $\mathcal{L}_\mathrm{E}$, and $\mathcal{L}_\mathrm{D}$).

2.3 Spatial pattern comparisons among M-, E-, and D-based diagnoses

It is not appropriate to directly compare the The TLMs are designed to highlight differences in L-A coupling strength between geographic regions and/or between different times of year in a given region. Those relative differences require subjective decisions to determine the threshold values separating regions of “strong” coupling from regions of weaker coupling. However, a direct comparison of the numerical values of TLMs based on different time windows of inputs (i.e., M, E, and D) is not appropriate for three primary reasons. First, the magnitude of the TLMs is strongly affected by the σ term (Eq. 1), and this measure of variability can be quite different for daytime and nighttime processes. For example, H_D has much larger variance than the H_ED-based H and P_{lcl} have much larger variances than that based on the entire-day-mean, which systematically enlarges the $\mathcal{L}_\mathrm{D}$ and $\mathcal{A}_\mathrm{D}$. Additionally, strong L-A coupling signals can be positive or negative, suggesting that in some cases the magnitude of TLMthe change of TLM’s magnitude (its absolute value) is the relevant quantity of interest rather than the magnitude of changes. Finally, L-A coupling processes are not characterized by clear thresholds, but rather by relative spatial and temporal differences.

To overcome these limitations and remove any subjectivity in our assessment of coupling strength, we use quantile to assess coupling strengths and to quantify the differences among quantify the spatial differences between $\mathrm{TLM_M}$, $\mathrm{TLM_E}$, and $\mathrm{TLM_D}$. For a specific TLM and a given quantile threshold, regions with absolute values of TLM over this threshold are marked for each of the M, the D, and the E cases. For the $\mathcal{A}_\mathrm{D}$ in summer a specific period for example, if the given threshold was is 0.8, grid cells with the top 20% largest $|\mathcal{A}|$ are marked. The ratio of the number of overlapping grid cells to the number of E-based marked grid cells is defined as the fitting rate between $\mathcal{A}_\mathrm{E}$ and $\mathcal{A}_\mathrm{D}$, which can reflect the difference between D- and E-based diagnoses at different levels of coupling strength. The same approach is applied to the legs in paired comparisons of E vs M, M vs D, and D vs E.

2.4 Signal attenuation from $\mathrm{TLM_E}$ to $\mathrm{TLM_M}$

The TLMs contain a correlation term ρ and a variance term σ (Eq. 1). First, we investigate the difference of the σ term between E- and M-based TLMs. To keep the symbols simple, we denote a_i and b_i (i is day index) as detrended and seasonal removed daily time series. A_j and B_j (j is the month index) are corresponding monthly time series. As the long-term average of b_i (i.e.,

$\bar{b}$) is zero, the σ_b can be expressed as

$$\sigma_b = \left(\frac{1}{DMY}\sum_{i=1}^{DMY} b_i^2 - \bar{b}^2\right)^{\frac{1}{2}}$$
$$= \left(\frac{1}{MY}\sum_{i=1}^{MY}\left[\frac{b_i^2 + b_{i+1}^2 + b_{i+2}^2 + ... + b_{i+D}^2}{D}\right]_j\right) \quad (4)$$

D, M, and Y are the number of days, months, and years, respectively. The σ_B can be written as

$$\sigma_{B_j} = \left(\frac{1}{MY}\sum_{j=1}^{MY} B_j^2 - \bar{B}^2\right)^{\frac{1}{2}}$$
$$= \left(\frac{1}{MY}\sum_{j=1}^{MY}\left(\frac{\sum_{i\in j}^{D} b_i}{D}\right)^2\right)^{\frac{1}{2}}$$
$$= \left(\frac{1}{MY}\sum_{j=1}^{MY}\left[\frac{(b_i + b_{i+1} + b_{i+2} + ... + b_{i+D})^2}{D^2}\right]_j\right)^{\frac{1}{2}} \quad (5)$$

σ_b contains all squared b_i, but σ_B contains averaged products of all combinations of b_i within a month. It is not difficult to proof that $D^2\sum_{i=1}^{N} b_i^2 \geq (b_i + b_{i+1} + ... + b_N)^2$. The equal relation stands when $b_i = b_{i+1} = ... = b_N$, indicating all daily variables are the same within a month. Considering all months, the σ_B is larger if b_i follows the Matthew principle better, that is large values assemble together in specific months and small values assemble together in other months. As b_i is a time series of variables in a natural process. b_i is somehow correlated with itself at a certain time scale, that is the memory of b_i. It implies that if b_i is large, its neighbours (e.g., b_{i-1} and b_{i+1}) are large as well. Thus, the memory (characterized by auto-correlation) may determine the information maintained from σ_b to σ_B, if the σ_b is considered as the accurate information we want.

The ρ term based on daily time series can be written as:

$$\rho(a,b) = \frac{\sum_{i=1}^{DMY}(a_i - \bar{a})\left(b_i - \bar{b}\right)}{\sigma_a \sigma_b}$$
$$= \frac{\sum_{i=1}^{DMY} a_i b_i}{\sigma_a \sigma_b}. \quad (6)$$

$\bar{a}$ and $\bar{b}$ are mean of a_i and b_i, respectively. Similarly, we can get $\rho(A,B)$ as

$$\rho(A,B) = \frac{\sum_{j=1}^{MY}\left(A_j - \bar{A}\right)\left(B_j - \bar{B}\right)}{\sigma_A \cdot \sigma_B}$$
$$= \frac{1}{\sigma_A \sigma_B}\sum_{j=1}^{MY}\left(\frac{\left(\sum_{i\in j} a_i\right)\left(\sum_{i\in j} b_i\right)}{D^2}\right). \quad (7)$$

The ρ term contains σ terms, which has been discussed. If we focus on the numerator, we can find that the difference of numerator between E and M has a similar structure as the ρ difference between E and M. Thus, we deduct that the cross-covariance between a_i and b_i is the key contributor to the difference of the ρ's numerator between E and M.

According to our deduction(see Supplementary Text 1), we infer that the memory of the L-A state (i.e., the auto-correlation for a single variable and the cross-covariance for paired variables) can characterize the coupling signal attenuation due to the monthly smoothing of daily time series. Thus, for a single variable (i.e., the σ term), we calculate its auto-correlation function (ACF) with a maximum lag 30 days (within a month). Then we average the ACF values belonging to the top 25% quantile as an indicator of the attenuation resistance (Supplementary Fig. S7)as an indicator of the loss rateS1a). And the attenuation rate resistance is characterized by the ratio of σ_{M} to σ_{E}. For paired variables (i.e., the numerator of the ρ term $N(\rho)$, e.g., $N(\rho)=\sum_{i=1}^{DMY} a_i b_i$ in Eq. 6), we calculate the cross-covariance function (CCF) instead, but with a maximum lag $\pm$30 days. For negatively correlated variables, we select the mean of the lowest 25% CCF as the indicator . (Supplementary Fig. S1b). For positively correlated variables, we select top 25% as the quantile threshold as the ACF case . (Supplementary Fig. S1c). Instead of $N(\rho_{\mathrm{M}})/N(\rho_{\mathrm{E}})$, we use $N(\rho_{\mathrm{M}})/(|N(\rho_{\mathrm{E}})|+|N(\rho_{\mathrm{M}})|)$ to characterize associated signal attenuation resistance, in order to avoid uncertainties due to phase shift from $N(\rho_{\mathrm{E}})$ to $N(\rho_{\mathrm{M}})$.

2.5 Δ|TLM| decomposition

According to the form of the coupling metrics (Eq. 1), the differences among $|\mathrm{TLM_M}|$, $|\mathrm{TLM_E}|$, and $|\mathrm{TLM_D}|$ can be decomposed as:

$$\begin{aligned}
\Delta|M| &= |M_2|-|M_1| \\
&= C_\rho + C_\sigma + C_{\sigma\rho} \\
C_\rho &= \sigma_1\left(|\rho_2|-|\rho_1|\right) \\
C_\sigma &= |\rho_1|\left(\sigma_2-\sigma_1\right) \\
C_{\sigma\rho} &= \left(|\rho_2|-|\rho_1|\right)\left(\sigma_2-\sigma_1\right).
\end{aligned}$$

using M_1 and M_2 are as specific TLMs based on two different time series. $\Delta|M|$:

$$\begin{aligned}
\Delta|M| &= |M_2|-|M_1| \\
&= C_\rho + C_\sigma + C_{\sigma\rho}, \text{where} \\
C_\rho &= \sigma_1\left(|\rho_2|-|\rho_1|\right) \\
C_\sigma &= |\rho_1|\left(\sigma_2-\sigma_1\right) \\
C_{\sigma\rho} &= \left(|\rho_2|-|\rho_1|\right)\left(\sigma_2-\sigma_1\right).
\end{aligned} \tag{8}$$

$\Delta|M|$ is the absolute value (coupling strength) shift from M_1 to M_2, which is composed of contributions from the correlation term (C_ρ), the fluctuation term (C_σ), and the joint term ($C_{\sigma\rho}$). Note that the three contributing terms may be either positive or negative. Thus, we take ~~absolute values of them~~ their absolute values to estimate their fractional contributions to the total coupling strength shift, $\Delta|M|$. ~~Taking the C_ρ as an example, its contribution~~ For example, the fractional contribution of the correlation term is calculated as:

$$\frac{|C_\rho|}{|C_\rho|+|C_\sigma|+|C_{\sigma\rho}|}. \tag{9}$$

2.6 Primary contributors to TLM pattern shift

~~The~~ As discussed in Section 2.3, describing TLMs with quantiles brings a focus to spatial patterns and regions of strong coupling, relative to neighboring regions. This approach can be extended to describe the shifts in spatial patterns from M_1 to M_2 ~~can be characterized by the change of quantile~~ using quantile changes (Δq)~~rather than by the~~. This is a better descriptor of changes in spatial patterns than Δ|TLM|, because the latter only quantifies the ~~values of ΔTLM~~ value changes within a specific grid cell, which cannot reflect the relative TLM change among grid cells. Moreover, within C_ρ, C_σ, and $C_{\sigma\rho}$, the largest contributor (Eq. 8 and 9) to Δ|TLM| may not be the dominant factor for Δq of specific grid cell. For example, one grid cell has a increase from $|M_1|$ to $|M_2|$ with $[C_\rho = 0, C_\sigma = 100, C_{\sigma\rho} = 20]$, but other grid cells has a increase with $[C_\rho = 0, C_\sigma = 100, C_{\sigma\rho} = 0]$. Obviously, the specific grid cell has a non-zero Δq. However, the component that determines q increase is not the largest contributor to $\Delta|M|$ (i.e., C_σ), but the $C_{\sigma\rho}$. The dominant factor of a specific grid cell must be the one without which the quantile of the grid cell has the lowest change from TLM_1 to TLM_2.

To demonstrate the dominant factor leading to Δq for a specific grid cell, we calculate Δq in four scenarios:

$$\begin{aligned}
\Delta q &= q_{|M_2|} - q_{|M_1|}\\
\Delta q_{\rho^-} &= q_{|M_2|-C_\rho} - q_{|M_1|}\\
\Delta q_{\sigma^-} &= q_{|M_2|-C_\sigma} - q_{|M_1|}\\
\Delta q_{\sigma\rho^-} &= q_{|M_2|-C_{\sigma\rho}} - q_{|M_1|}.
\end{aligned} \tag{10}$$

Δq is the q shift of a specific grid cell from $|M_1|$ to $|M_2|$. Δq_{ρ^-} is the q shift without the contribution of the ρ term (i.e., from $|M_1|$ to $|M_2| - C_\rho$). Similar definitions are applied for Δq_{σ^-} and $\Delta q_{\sigma\rho^-}$. Then we can demonstrate the dominant factor for a specific grid cell as:

$$\begin{aligned}
&f_{\min}\left(\Delta q_{\rho^-}, \Delta q_{\sigma^-}, \Delta q_{\sigma\rho^-}\right), \text{ if } \Delta q > 0,\\
&f_{\max}\left(\Delta q_{\rho^-}, \Delta q_{\sigma^-}, \Delta q_{\sigma\rho^-}\right), \text{ if } \Delta q < 0.
\end{aligned} \tag{11}$$

$f_{\min}$ ($f_{\max}$) is a function selecting the corresponding subscript of the term with the minimum (maximum) value.

3 Results

3.1 Spatial pattern differences among diagnoses based on $\mathrm{TLM_M}$, $\mathrm{TLM_E}$, and $\mathrm{TLM_D}$

~~By using~~ Using ERA5 hourly data, we generated three homologous time series ~~by varied~~ with three different temporal averaging algorithms: monthly mean (M), entire-day-mean (E), and daytime-mean (D)~~, which~~. These three time series were used to estimate the coupling strength between ~~land and~~ the land and the atmosphere based on the two-legged metrics (Eq. 3, ~~see~~ Sect. 2.2). Figure 1 assesses the geographic consistency between the coupling strengths determined by the three different time series by showing the fitting rate of a suite of comparisons at different levels of quantile thresholds (~~see~~ Sect. 2.3). In all seasons, $\mathcal{A}$ has a much lower fitting rate than $\mathcal{L}$, and the fitting rate of $\mathcal{T}$ lies between the two. This is a reflection of the long memory inherent in the land relative to the atmosphere. In addition, fitting rates varies with season, and JJA has the lowest value, indicating that the largest spatial difference occurs in the summer of the Northern Hemisphere where most land is located. The median of fitting rates over all legs and seasons is 69.4% if the largest 10% of TLM values are considered physically significant, demonstrating that the determination of L-A coupling strongly depends on the averaging time period of the input time series. Most fitting rates decrease with the rise of the quantile threshold, and the lowest fitting rate is 15.2% ($\mathcal{A}_{\mathrm{M}}$ vs. $\mathcal{A}_{\mathrm{D}}$ in JJA for the 0.95 quantile threshold), indicating that ~~a minor~~ only a small portion of the most strongly coupled regions (the top 5%) are simultaneously diagnosed by both D and M. ~~In all seasons, $\mathcal{A}$ has a much lower fitting rate than $\mathcal{L}$, and the fitting rate of $\mathcal{T}$ lies between the two. In addition, fitting rates are generally lower during JJA than in other seasons. Thus, to avoid a repetitive presentation of all results~~To focus on the season and coupling leg with the largest sensitivity to time series averaging window, we select $\mathcal{A}$ in summer (JJA and DJF in the Northern and Southern Hemisphere, respectively) as an example to explore the TLM differences in the following content.

Figure 2a illustrates the differences of strong L-A coupling regions (90% quantile as the threshold) among $\mathcal{A}_{\mathrm{M}}$, $\mathcal{A}_{\mathrm{D}}$, and $\mathcal{A}_{\mathrm{E}}$ during ~~summer~~each hemisphere's summer season. Although the total ~~overlap area~~ area of overlap ($\mathcal{A}_{\mathrm{M}} \cap \mathcal{A}_{\mathrm{E}} \cap \mathcal{A}_{\mathrm{D}}$, pale taupe area in Fig. 2a) accounts for approximately 50% of strong coupling regions, vast disagreement among those diagnoses still exists especially in the Northern Hemisphere. $\mathcal{A}_{\mathrm{M}}$ suggests strong coupling in some climate transition regions (such as the western and southern US, central Asia, northern India, eastern Sahel, and southern Australia). $\mathcal{A}_{\mathrm{E}}$ highlights some mid-latitude regions, such as the southwestern ~~and southeastern~~ US, a part of the Sahara, Arabia, central India, and northwestern China. However, as the most accurate diagnosis, $\mathcal{A}_{\mathrm{D}}$ demonstrates that the L-A coupling is stronger in the southeastern US and in high latitudes, such as the boreal forest region of Canada, and parts of northern Eurasia. Interestingly, the fraction of $\mathcal{A}_{\mathrm{M}} \cap \mathcal{A}_{\mathrm{D}}$ (1.7%) is much less than that of $\mathcal{A}_{\mathrm{M}} \cap \mathcal{A}_{\mathrm{E}}$ (7.6%) or $\mathcal{A}_{\mathrm{E}} \cap \mathcal{A}_{\mathrm{D}}$ (11.5%), implying that $\mathcal{A}_{\mathrm{E}}$ is the intermediate status between $\mathcal{A}_{\mathrm{M}}$ and $\mathcal{A}_{\mathrm{D}}$. Therefore, we investigate the two-stepped transitions: $\mathcal{A}_{\mathrm{M}} \rightarrow \mathcal{A}_{\mathrm{E}}$ (M vs E) and $\mathcal{A}_{\mathrm{E}} \rightarrow \mathcal{A}_{\mathrm{D}}$ (E vs D) in the following analysis.

Figure 2b shows the quantile transition of $\mathcal{A}_{\mathrm{M}} \rightarrow \mathcal{A}_{\mathrm{E}}$ in summer. Two types of regions are important. One is the green/yellow regions showing quantile shifts within the strongest coupling group, which coincide with the regions highlighted by Fig. 2a. The other is the dark blue/red regions, indicating the largest quantile changes from $\mathcal{A}_{\mathrm{M}}$ to $\mathcal{A}_{\mathrm{E}}$. Interestingly, the quantile drops dramatically in the center of North America, the Sahel, and central Asia. On one hand, those $\mathcal{A}_{\mathrm{M}}$ diagnosed strongly L-A coupled regions agree with the findings from Koster et al. (2004) that was based on six-day averaged data. On the other hand, the coupling strength of those regions fades significantly when E-based diagnoses are applied. For instance, the quantile for three selected sites in these areas (red triangles in Fig. 2b) drops from $> 80\%$ ($\mathcal{A}_{\mathrm{M}}$) to $< 30\%$ ($\mathcal{A}_{\mathrm{E}}$). It indicates that the L-A coupling strength may be overestimated in those climatic transition zones if multi-day average data was applied. In the next section, we will demonstrate the mechanism resulting in such vast differences between $\mathcal{A}_{\mathrm{M}}$ and $\mathcal{A}_{\mathrm{E}}$.

Figure 2c displays the quantile transition of $\mathcal{A}_{\mathrm{E}}\rightarrow\mathcal{A}_{\mathrm{D}}$ in summer. In general, the most significant quantile shifts occur in the Northern Hemisphere and the strongly coupled regions are diagnosed further north by $\mathcal{A}_{\mathrm{D}}$. The Sahara and Arabia contribute the largest quantile drop of $\mathcal{A}_{\mathrm{E}}\rightarrow\mathcal{A}_{\mathrm{D}}$. Some regions show strong coupling based on both $\mathcal{A}_{\mathrm{E}}$ and $\mathcal{A}_{\mathrm{D}}$. However, their coupling strength is overestimated by $\mathcal{A}_{\mathrm{E}}$, such as the southwestern US and northern Mexico, India, and northwestern China. Key regions with increasing $\mathcal{A}$ quantile include the eastern US, boreal forests of Canada, northern Eurasia, and northeastern China.

3.2 M vs E

Through analyzing the formulas of $\mathrm{TLM_E}$ and $\mathrm{TLM_M}$ (~~see Supplementary Text 1~~Sect. 2.4), we demonstrate that both the σ term and the numerator of the ρ term (denoted by $N(\rho)$) attenuate from $\mathrm{TLM_E}$ to $\mathrm{TLM_M}$. The decreasing rate relies on the contrast between the variation of daily elements within the same month and the variation of daily elements across months. Furthermore, we infer that the memory of specific E time series (i.e., $\overline{\mathrm{ACF}}_{>75\%}$) or paired E time series (i.e., $\overline{\mathrm{CCF}}_{>75\%}$ and $\overline{\mathrm{CCF}}_{<25\%}$ for positively and negatively correlated pairs, respectively) can be an indicator characterizing the coupling signal loss from E to M~~(see Sect. 2.4).~~.

Figure 3 verifies our deduction by showing ~~high~~ statistically significant correlations between the coupling signal loss rate and the indicator regarding L-A memory. ~~Significant~~ These significant correlation coefficients suggest that our indicator ~~adequately explains the attenuation of the coupling signal~~ can capture the global pattern of coupling signal attenuation due to monthly smoothing. Specifically, regions with higher auto-correlation between individual days lead to a smaller loss of information when a daily time series is converted to a monthly time series. In the negative pair case (Fig. 3d), the indicator sensitivity to the signal attenuation may be weakened. The primary distractors (top and bottom-right regions isolated by blue lines in Fig. 3d) are from areas with extreme climate conditions, such as Greenland, Sahara, and Arabia (Fig. 3f). Nevertheless, the ~~moderately large~~ significance of the correlation coefficient suggests that the indicator is still able to reflect the attenuation ~~process~~magnitude. Surprisingly, the indicator captures not only the signal attenuation, but also phase shifts (the negative quadrant in Fig. 3e).

Through Figure 3, we demonstrate that $\mathrm{TLM_M}$ loses L-A coupling signal as a result of smoothing the E time series and the memory of L-A states ~~determines the attenuation rate~~significantly affect the attenuation process. Although memory is another facet of ~~system~~ coupling at the seasonal scale (Dirmeyer et al., 2009, 2016, 2018; Guo et al., 2011), it is not the main focus of TLM diagnosing the inter-daily L-A interactions. Moreover, two types of ~~memories~~ memory (auto-correlation of a single variable and cross-covariance of coupled variables~~, Supplementary Eq. S8 and S9~~) jointly influence the $\mathrm{TLM_M}$ in the form of the quotient (Eq. 6 and 7), which increases the uncertainty of $\mathrm{TLM_M}$ reflecting the signal of local L-A memory. Thus, ~~we conclude that~~ the diagnoses based on $\mathrm{TLM_M}$ are obscured by the varied memories of L-A state, ~~which is not clearly represented~~

~~in the TLM_M and is not the primary feature to be dug out~~leading to a bias in the discovered hot spots of L-A coupling. Some regions with strong L-A coupling but low L-A memory (i.e., large daily fluctuations) may be overlooked by TLM_M.

3.3 E vs D

The value of $|\mathcal{L}_\text{D}|$ is larger than $|\mathcal{L}_\text{E}|$ worldwide (Supplementary Fig. S2a), and the primary contributor is the variability (C_σ, Fig. 4a~~, see Sect. ??~~). But the universal increase of C_σ is not always the key driver of spatial pattern differences between $\mathcal{L}_\text{E}$ and $\mathcal{L}_\text{D}$ (Fig. 4c). For instance, both $\mathcal{L}_\text{E}$ and $\mathcal{L}_\text{D}$ suggest a portion of middle and high latitude regions of the Northern Hemisphere with strong soil moisture-sensible heat flux (θ–H) coupling (Supplementary Fig. S3). However, different from $\mathcal{L}_\text{E}$, $\mathcal{L}_\text{D}$ suggests stronger coupling in North America than in Eurasia, which is primarily caused by the change of ρ (C_ρ and $C_{\sigma\rho}$). This difference is caused by the time averaging algorithm of the E time series, which considers one day from 0:00 to 24:00 based on Coordinated Universal Time (UTC). Thus, the E averaging period in the Western Hemisphere starts at night and ends on the following day. The opposite is true for the Eastern Hemisphere (left panel of Fig. 4e). However, in a large region of North America, the nighttime soil moisture θ_N is more correlated to the daytime soil moisture θ_N of the previous day than the next day (Supplementary Fig. ~~S5~~S4). Thus the entire-day average in the Western Hemisphere dramatically flattens the inter-daily fluctuations of soil moisture, leading to an underestimation of $\rho(\theta, H)$ by E. The right panel of Figure 4e shows that in a selected area of North America, the difference between E- and D- based $\rho(\theta, H)$ is significantly reduced if the θ_E was calculated by averaging the θ_D and the following θ_N.

Figure 4b shows that both C_σ and the C_ρ can be important for $\Delta|\mathcal{A}|$ from E to D. C_σ is likely the main contributor in humid regions, while the C_ρ dominates arid and semi-arid areas. Figure 4d illustrates that C_σ is the primary contributor to quantile increase in most strong $\mathcal{A}$ regions (yellow areas in Figure 2c). However, in fact, their quantile increase is caused by the quantile decrease in the Sahara and Arabia (Supplementary Fig. S2b), where $\mathcal{A}$ is negative (Supplementary the second row of Fig. ~~S4~~S5). As $\mathcal{A}_\text{D}$ is universally higher than $\mathcal{A}_\text{E}$, the coupling strength over the Sahara and Arabia is weakened.

Generally, the land surface is the source of heating for the lower atmosphere during the day. Driven by the surface temperature T_s, H heats the air and grows the height of the PBL (left panel of Fig. 4f), leading to positive $\rho(H, T_\text{2m})$ and $\rho(H, P_\text{lcl})$. However, the climate of the Sahara and Arabia is likely dominated by another mechanism. Over the northern Sahara, for instance, atmospheric advection seems to be the primary driver of inter-daily variations of near-surface atmospheric states (i.e., both T_2m and D_2m) instead of the surface (middle panel of Fig. 4f, see Supplementary Text~~ 2~~). A key consequence is that the T_2m is no longer a passive variable, but drives the H fluctuation (right panel of Fig. 4f), resulting in a negative $\rho(H, T_\text{2m})$ and further a negative $\rho(H, P_\text{lcl})$. In fact, both the bottom-up heating and the advection-driven heating mechanisms (left and middle panel of Fig. 4f) affect the climate variations in this region. However, the former only occurs during the daytime, while the latter can exist throughout a day. In comparison to E, the D averaging approach can minimize the effect of the former in L-A diagnoses.

4 Discussion

We demonstrate that the use of both monthly-mean and entire-day-mean daily data may result in biases in the diagnosis of L-A coupling. By comparing the two-legged metrics (TLM) calculated by the monthly (M), the daytime-only-mean (D), and entire-day-mean (E) time series, we found that the coverage discrepancy of their spatial patterns of strong coupling can be as large as 84.8% (Fig. 1). The diagnostic uncertainties introduced through monthly smoothing (i.e., differences between TLM_E and TLM_M) are determined by the persistence or memory of local L-A states, which may result in the overestimation of L-A coupling strength in some climatic transition zones ~~(Koster et al., 2004)~~where climatic inter-monthly variations are larger than intra-monthly variations. Furthermore, we have demonstrated that integrating nighttime information in L-A diagnoses (i.e., TLM_E) may incorporate confounding effects from other mechanisms.

Although monthly-based and daily-based correlation coefficients capture the synchronized fluctuations of two variables from different perspectives, their linkage is yet unclear. In this study, for the first time as far as we know, we demonstrate how the correlation is weakened by monthly smoothing mathematically. Moreover, we propose indicators based on the auto-correlation function and cross-correlation function representing L-A memory to characterize the information loss. And these indicators are able to capture the information loss worldwide regardless of geophysical and atmospheric complexities (Fig. 3). In addition, these indicators first link the memory of time series to the correlation attenuation due to coarser temporal smoothing, which has potential implications in broad fields.

Two mechanisms obscuring L-A diagnoses are discovered for the first time in our study, which again reflects the crucial need for daytime-only-mean data. First, atmospheric advection may dominate the daily fluctuations of both sensible heat flux and the LCL height in the Sahara and Arabia, resulting in a spurious negative relationship between the two. In comparison to highlighting these trivial regions by daily data-based diagnosis, daytime-only-mean data can make the diagnosis prevent the pitfall. Second, the traditional entire-day-mean daily data is obtained by averaging over 24 hours based on the UTC. It emphasizes shifted diurnal cycles according to longitude, which may mask signals of land state fluctuation in the Western Hemisphere, and provide inconsistent comparisons with the Eastern Hemisphere.

Land-atmosphere interactions have been demonstrated to be a key element in understanding climate dynamics (Berg et al., 2017; Findell et al., 2015; Humphrey et al., 2021; Koster et al., 2004; Seneviratne et al., 2010; Taylor et al., 2012). Different from simple causality, the land and the atmosphere are highly coupled by multiple variables that interact with each other (Santanello et al., 2018; Seneviratne et al., 2010), which raises difficulties for the understanding and simulation of relevant processes (Taylor et al., 2012, 2017). To investigate the complex coupled system, we must characterize its behaviors under various conditions and reveal relevant physical processes. Thus, a suite of metrics has been proposed to detect the features of a specific process (Santanello et al., 2018) based on either physical or statistical perspectives (https://www.pauldirmeyer.com/coupling-metrics). ~~Moreover, these~~ These metrics are helpful to evaluate model ~~performances~~ performance either against observations or through model inter-comparisons, and further support model improvements. However, it is rare to find datasets providing the required complete fields of high-frequency (≤ 3 hours) outputs for L-A investigations. For instance, daily data is generally the highest frequency output provided by numerous model inter-comparison projects (e.g., ~~(Eyring et al., 2016; Warszawski et al., 2014)~~Eyring et al. (2016); Warszawski et al. (2014)), which is not adequate to diagnose the performance of Earth system models (ESMs) in simulating L-A interactions. Moreover, our study demonstrates that even daily data may overlook some important L-A patterns due to the ~~effects~~ perturbations of other processes. ~~The daytime-only-mean daily data used in our study is an average of time steps within the nine hours centered on local noon, whereas the traditional entire-day-mean daily data is obtained by averaging over 24 hours based on the UTC. Thus the latter emphasizes shifted diurnal cycles according to longitude, which may mask signals of land state fluctuation in the Western Hemisphere, and provide inconsistent comparisons with the Eastern Hemisphere.~~

Therefore, we call for careful attention to the requirements of high-frequency data in terms of diurnal cycle investigations, whose diagnoses can further reinforce ESM skills in predicting future climate under different scenarios. Assuredly, storage is a bottleneck for producing and sharing high-frequency data. Thus, we propose two approaches to balance the cost of storage and the need for high-frequency data. One approach is to integrate process-based metrics within ESMs so that the metric values themselves can be saved as model output, rather than calculated *a posteriori* (Findell and Eltahir, 2003a, b; Santanello et al., 2009; Tawfik and Dirmeyer, 2014). Therefore the ~~diagnosis~~ diagnostic information can be easily collected at the cost of only a little extra computing time. The other is to generate different types of daily model output for different research purposes. In addition to daytime mean values, separate averages throughout the local morning, midday, afternoon, and nighttime would be interesting as well depending on the specific perspectives of interest (Taylor et al., 2012; Guillod et al., 2015). Such averaging algorithms must depend on the local time rather than the UTC, and the varied daytime length according to latitude and time of year should be considered.

5 Conclusions

This study demonstrates that the use of monthly or entire-day-mean daily data may lead to uncertainties in diagnoses of land-atmosphere (L-A) coupling strength and interactions. The arithmetic mean of time series including the nighttime weakens the signal of L-A coupling. And the spatial heterogeneity of such weakening effects can alter the diagnosis of coupling strength based on the two-legged metrics. In addition, two phenomena were discovered, which can dramatically obscure the L-A diagnoses if the entire-day-mean daily time series is applied. One is a spurious relationship between flux and atmosphere states led by atmospheric advection in Sahara and Arabia. The other is the underestimation of L-A coupling in the Western Hemisphere due to the classical daily averaging algorithm based on the Coordinated Universal Time that twists the segmentation of the diurnal cycle. Through this study, we call ~~for~~ attention to the requirements of high-frequency data for L-A diagnoses. L-A metrics can be either integrated within Earth System Models to avoid huge storage for high-frequency outputs or fed by outputs averaging over the sub-daily period of interest. Either of the approaches can improve the accuracy of L-A diagnoses with minimal cost of computing time and storage space.

Code and data availability. The 0.5° ERA5 data is available at https://cds.climate.copernicus.eu/#!/home. The code for calculating the two-legged metrics can be found via http://www.coupling-metrics.com.

Author contributions. Z.Y., K.F., E.S., and S.M. conceived the research question; Z.Y. and K.F. designed the research; Z.Y. and N.R. collected and processed the data; Z.Y. performed the research; Z.Y. drafted the manuscript; all authors interpreted results and contributed to the editing.

Competing interests. The authors declare no competing interests.

Acknowledgements. Z.Y. and K.~~F~~G. are supported by CIMES grant NA18OAR4320123. P.D. is supported by NOAA grant NA19OAR4310242. Yujin Zeng and Jing Feng are acknowledged for their comments and suggestions on an internal review of the manuscript. We acknowledge GFDL resources made available for this research. We thank the European Centre for Medium-Range Weather Forecasts (ECMWF) for providing the ERA5 data. We thank the editor and two anonymous referees for their helpful comments and efforts.

References

Berg, A., Lintner, B., Findell, K., and Giannini, A.: Soil Moisture Influence on Seasonality and Large-Scale Circulation in Simulations of the West African Monsoon, Journal of Climate, 30, 2295–2317, https://doi.org/10.1175/JCLI-D-15-0877.1, 2017.

Chen, L. and Dirmeyer, P. A.: Impacts of Land-Use/Land-Cover Change on Afternoon Precipitation over North America, Journal of Climate, 30, 2121–2140, https://doi.org/10.1175/JCLI-D-16-0589.1, 2017.

Dirmeyer, P. A.: The terrestrial segment of soil moisture-climate coupling, Geophysical Research Letters, 38, n/a–n/a, https://doi.org/10.1029/2011GL048268, 2011.

Dirmeyer, P. A., Schlosser, C. A., and Brubaker, K. L.: Precipitation, recycling, and land memory: An integrated analysis, Journal of Hydrometeorology, 10, 278–288, https://doi.org/10.1175/2008JHM1016.1, 2009.

Dirmeyer, P. A., Cash, B. A., Kinter, J. L., Stan, C., Jung, T., Marx, L., Towers, P., Wedi, N., Adams, J. M., Altshuler, E. L., Huang, B., Jin, E. K., and Manganello, J.: Evidence for enhanced land-atmosphere feedback in a warming climate, Journal of Hydrometeorology, 13, 981–995, https://doi.org/10.1175/JHM-D-11-0104.1, 2012.

Dirmeyer, P. A., Wang, Z. Y., Mbuh, M. J., and Norton, H. E.: Intensified land surface control on boundary layer growth in a changing climate, Geophysical Research Letters, 41, 1290–1294, https://doi.org/10.1002/2013GL058826, 2014.

Dirmeyer, P. A., Wu, J., Norton, H. E., Dorigo, W. A., Quiring, S. M., Ford, T. W., Santanello, J. A., Bosilovich, M. G., Ek, M. B., Koster, R. D., Balsamo, G., and Lawrence, D. M.: Confronting Weather and Climate Models with Observational Data from Soil Moisture Networks over the United States, Journal of Hydrometeorology, 17, 1049–1067, https://doi.org/10.1175/JHM-D-15-0196.1, 2016.

Dirmeyer, P. A., Chen, L., Wu, J., Shin, C. S., Huang, B., Cash, B. A., Bosilovich, M. G., Mahanama, S., Koster, R. D., Santanello, J. A., Ek, M. B., Balsamo, G., Dutra, E., and Lawrence, D. M.: Verification of land-atmosphere coupling in forecast models, reanalyses, and land surface models using flux site observations, Journal of Hydrometeorology, 19, 375–392, https://doi.org/10.1175/JHM-D-17-0152.1, 2018.

Dirmeyer, P. A., Balsamo, G., Blyth, E. M., Morrison, R., and Cooper, H. M.: Land-Atmosphere Interactions Exacerbated the Drought and Heatwave Over Northern Europe During Summer 2018, AGU Advances, 2, https://doi.org/10.1029/2020av000283, 2021.

Eyring, V., Bony, S., Meehl, G. A., Senior, C. A., Stevens, B., Stouffer, R. J., and Taylor, K. E.: Overview of the Coupled Model Intercomparison Project Phase 6 (CMIP6) experimental design and organization, Geoscientific Model Development, 9, 1937–1958, https://doi.org/10.5194/gmd-9-1937-2016, 2016.

Ferguson, C. R., Wood, E. F., and Vinukollu, R. K.: A Global intercomparison of modeled and observed land-atmosphere coupling, Journal of Hydrometeorology, 13, 749–784, https://doi.org/10.1175/JHM-D-11-0119.1, 2012.

Findell, K. L. and Eltahir, E. A. B.: Atmospheric Controls on Soil Moisture–Boundary Layer Interactions. Part I: Framework Development, Journal of Hydrometeorology, 4, 552–569, https://doi.org/10.1175/1525-7541(2003)004<0552:ACOSML>2.0.CO;2, 2003a.

Findell, K. L. and Eltahir, E. A. B.: Atmospheric controls on soil moisture-boundary layer interactions: Three-dimensional wind effects, Journal of Geophysical Research: Atmospheres, 108, 1–21, https://doi.org/10.1029/2001jd001515, 2003b.

Findell, K. L., Gentine, P., Lintner, B. R., and Kerr, C.: Probability of afternoon precipitation in eastern United States and Mexico enhanced by high evaporation, Nature Geoscience, 4, 434–439, https://doi.org/10.1038/ngeo1174, 2011.

Findell, K. L., Gentine, P., Lintner, B. R., and Guillod, B. P.: Data Length Requirements for Observational Estimates of Land–Atmosphere Coupling Strength, Journal of Hydrometeorology, 16, 1615–1635, https://doi.org/10.1175/JHM-D-14-0131.1, 2015.

Findell, K. L., Keys, P. W., van der Ent, R. J., Lintner, B. R., Berg, A., and Krasting, J. P.: Rising Temperatures Increase Importance of Oceanic Evaporation as a Source for Continental Precipitation, Journal of Climate, 32, 7713–7726, https://doi.org/10.1175/JCLI-D-19-0145.1, 2019.

Georgakakos, K. P. and Bras, R. L.: A hydrologically useful station precipitation model: 1. Formulation, Water Resources Research, 20, 1585–1596, https://doi.org/10.1029/WR020i011p01585, 1984.

Guillod, B. P., Orlowsky, B., Miralles, D., Teuling, A. J., Blanken, P. D., Buchmann, N., Ciais, P., Ek, M., Findell, K. L., Gentine, P., Lintner, B. R., Scott, R. L., den Hurk, B. V., and Seneviratne, S. I.: Land-surface controls on afternoon precipitation diagnosed from observational data: uncertainties and confounding factors, Atmospheric Chemistry and Physics, 14, 8343–8367, https://doi.org/10.5194/acp-14-8343-2014, 2014.

Guillod, B. P., Orlowsky, B., Miralles, D. G., Teuling, A. J., and Seneviratne, S. I.: Reconciling spatial and temporal soil moisture effects on afternoon rainfall, Nature Communications, 6, 6443, https://doi.org/10.1038/ncomms7443, 2015.

Guo, Z., Dirmeyer, P. A., and Delsole, T.: Land surface impacts on subseasonal and seasonal predictability, Geophysical Research Letters, 38, https://doi.org/10.1029/2011GL049945, 2011.

Guo, Z. C., Dirmeyer, P. A., Koster, R., Sud, Y. C., Bonan, G., Oleson, K. W., Chan, E., Verseghy, D., Cox, P., Gordon, C. T., McGregor, J. L., Kanae, S., Kowalczyk, E., Lawrence, D., Liu, P., Mocko, D., Lu, C. H., Mitchell, K., Malyshev, S., McAvaney, B., Oki, T., Yamada, T., Pitman, A., Taylor, C. M., Vasic, R., and Xue, Y. K.: GLACE: The Global Land–Atmosphere Coupling Experiment. Part II: Analysis, Journal of Hydrometeorology, 7, 611–625, https://doi.org/10.1175/JHM511.1, 2006.

Hersbach, H., Bell, B., Berrisford, P., Biavati, G., Horanyi, A., Sabater, J. M., Nicolas, J., Peubey, C., Radu, R., Rozum, I., Schepers, D., Simmons, A., Soci, C., Dee, D., and Thepaut, J.-N.: ERA5 hourly data on pressure levels from 1979 to present, https://doi.org/10.24381/cds.adbb2d47, 2018.

Hersbach, H., Bell, B., Berrisford, P., Hirahara, S., Horányi, A., Muñoz-Sabater, J., Nicolas, J., Peubey, C., Radu, R., Schepers, D., Simmons, A., Soci, C., Abdalla, S., Abellan, X., Balsamo, G., Bechtold, P., Biavati, G., Bidlot, J., Bonavita, M., Chiara, G. D., Dahlgren, P., Dee, D., Diamantakis, M., Dragani, R., Flemming, J., Forbes, R., Fuentes, M., Geer, A., Haimberger, L., Healy, S., Hogan, R. J., Hólm, E., Janisková, M., Keeley, S., Laloyaux, P., Lopez, P., Lupu, C., Radnoti, G., de Rosnay, P., Rozum, I., Vamborg, F., Villaume, S., and Thépaut, J. N.: The ERA5 global reanalysis, Quarterly Journal of the Royal Meteorological Society, 146, 1999–2049, https://doi.org/10.1002/qj.3803, 2020.

Hu, H., Leung, L. R., and Feng, Z.: Early warm-season mesoscale convective systems dominate soil moisture–precipitation feedback for summer rainfall in central United States, Proceedings of the National Academy of Sciences, 118, e2105260118, https://doi.org/10.1073/pnas.2105260118, 2021.

Humphrey, V., Berg, A., Ciais, P., Gentine, P., Jung, M., Reichstein, M., Seneviratne, S. I., and Frankenberg, C.: Soil moisture–atmosphere feedback dominates land carbon uptake variability, Nature, 592, 65–69, https://doi.org/10.1038/s41586-021-03325-5, 2021.

Jach, L., Schwitalla, T., Branch, O., Warrach-Sagi, K., and Wulfmeyer, V.: Sensitivity of land–atmosphere coupling strength to changing atmospheric temperature and moisture over Europe, Earth System Dynamics, 13, 109–132, https://doi.org/10.5194/esd-13-109-2022, 2022.

Klein, C. and Taylor, C. M.: Dry soils can intensify mesoscale convective systems, Proceedings of the National Academy of Sciences of the United States of America, 117, 21 132–21 137, https://doi.org/10.1073/pnas.2007998117, 2020.

Koster, R. D., Dirmeyer, P. A., Guo, Z., Bonan, G., Chan, E., Cox, P., Gordon, C. T., Kanae, S., Kowalczyk, E., Lawrence, D., Liu, P., Lu, C. H., Malyshev, S., McAvaney, B., Mitchell, K., Mocko, D., Oki, T., Oleson, K., Pitman, A., Sud, Y. C., Taylor, C. M., Verseghy, D., Vasic, R., Xue, Y., and Yamada, T.: Regions of strong coupling between soil moisture and precipitation, Science, 305, 1138–1140, https://doi.org/10.1126/science.1100217, 2004.

Koster, R. D., Sud, Y. C., Guo, Z. C., Dirmeyer, P. A., Bonan, G., Oleson, K. W., Chan, E., Verseghy, D., Cox, P., Davies, H., Kowalczyk, E., Gordon, C. T., Kanae, S., Lawrence, D., Liu, P., Mocko, D., Lu, C. H., Mitchell, K., Malyshev, S., McAvaney, B., Oki, T., Yamada, T., Pitman, A., Taylor, C. M., Vasic, R., and Xue, Y. K.: GLACE: The Global Land–Atmosphere Coupling Experiment. Part I: Overview, Journal of Hydrometeorology, 7, 590–610, https://doi.org/10.1175/JHM510.1, 2006.

Laguë, M. M., Bonan, G. B., and Swann, A. L. S.: Separating the Impact of Individual Land Surface Properties on the Terrestrial Surface Energy Budget in both the Coupled and Uncoupled Land–Atmosphere System, Journal of Climate, 32, 5725–5744, https://doi.org/10.1175/JCLI-D-18-0812.1, 2019.

Lorenz, R., Pitman, A. J., Hirsch, A. L., and Srbinovsky, J.: Intraseasonal versus interannual measures of land-atmosphere coupling strength in a global climate model: GLACE-1 versus GLACE-CMIP5 experiments in ACCESS1.3b, Journal of Hydrometeorology, 16, 2276–2295, https://doi.org/10.1175/JHM-D-14-0206.1, 2015.

Miralles, D. G., Gentine, P., Seneviratne, S. I., and Teuling, A. J.: Land-atmospheric feedbacks during droughts and heatwaves: state of the science and current challenges, Annals of the New York Academy of Sciences, 1436, 19–35, https://doi.org/10.1111/nyas.13912, 2019.

Santanello, J. A., Peters-Lidard, C. D., Kumar, S. V., Alonge, C., and Tao, W. K.: A Modeling and Observational Framework for Diagnosing Local Land–Atmosphere Coupling on Diurnal Time Scales, Journal of Hydrometeorology, 10, 577–599, https://doi.org/10.1175/2009JHM1066.1, 2009.

Santanello, J. A., Dirmeyer, P. A., Ferguson, C. R., Findell, K. L., Tawfik, A. B., Berg, A., Ek, M., Gentine, P., Guillod, B. P., van Heerwaarden, C., Roundy, J., and Wulfmeyer, V.: Land–Atmosphere Interactions: The LoCo Perspective, Bulletin of the American Meteorological Society, 99, 1253–1272, https://doi.org/10.1175/BAMS-D-17-0001.1, 2018.

Schumacher, D. L., Keune, J., van Heerwaarden, C. C., de Arellano, J. V.-G., Teuling, A. J., and Miralles, D. G.: Amplification of mega-heatwaves through heat torrents fuelled by upwind drought, Nature Geoscience, 12, 712–717, https://doi.org/10.1038/s41561-019-0431-6, 2019.

Seneviratne, S. I., Corti, T., Davin, E. L., Hirschi, M., Jaeger, E. B., Lehner, I., Orlowsky, B., and Teuling, A. J.: Investigating soil moisture–climate interactions in a changing climate: A review, Earth-Science Reviews, 99, 125–161, https://doi.org/10.1016/j.earscirev.2010.02.004, 2010.

Tawfik, A. B. and Dirmeyer, P. A.: A process-based framework for quantifying the atmospheric preconditioning of surface-triggered convection, Geophysical Research Letters, 41, 173–178, https://doi.org/10.1002/2013GL057984, 2014.

Taylor, C. M., de Jeu, R. A. M., Guichard, F., Harris, P. P., and Dorigo, W. A.: Afternoon rain more likely over drier soils, Nature, 489, 423–426, https://doi.org/10.1038/nature11377, 2012.

Taylor, C. M., Belušić, D., Guichard, F., Parker, D. J., Vischel, T., Bock, O., Harris, P. P., Janicot, S., Klein, C., and Panthou, G.: Frequency of extreme Sahelian storms tripled since 1982 in satellite observations, Nature, 544, 475–478, https://doi.org/10.1038/nature22069, 2017.

Warszawski, L., Frieler, K., Huber, V., Piontek, F., Serdeczny, O., and Schewe, J.: The Inter-Sectoral Impact Model Intercomparison Project (ISI–MIP): Project framework, Proceedings of the National Academy of Sciences, 111, 3228–3232, https://doi.org/10.1073/pnas.1312330110, 2014.

Zhou, S., Williams, A. P., Lintner, B. R., Berg, A. M., Zhang, Y., Keenan, T. F., Cook, B. I., Hagemann, S., Seneviratne, S. I., and Gentine, P.: Soil moisture–atmosphere feedbacks mitigate declining water availability in drylands, Nature Climate Change, https://doi.org/10.1038/s41558-020-00945-z, 2021.

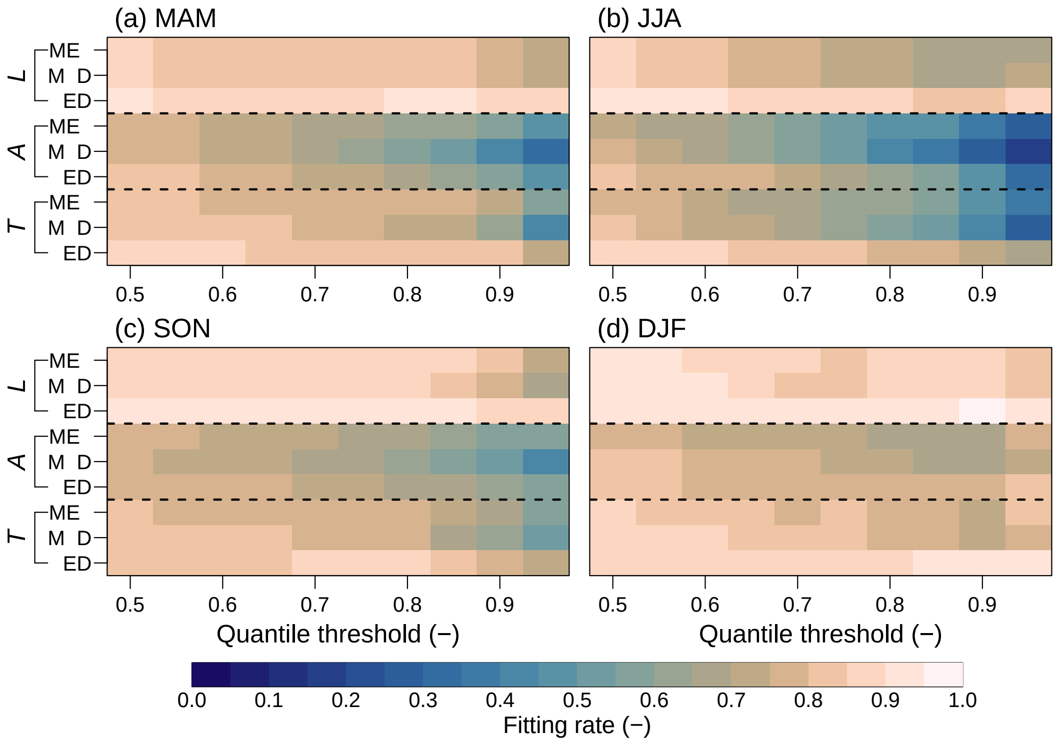

Figure 1. Fitting rates of different paired comparisons as a function of quantile threshold by using global data (see Sect. 2.3). The subplots represent different seasons. The three bands (separated by dashed lines) in each subplot indicate the land leg ($\mathcal{L}$), the atmospheric leg ($\mathcal{A}$), and the total ($\mathcal{T}$). Within each band; the three rows represent three paired comparisons, they are (from top to bottom) M vs E, M vs D, and E vs D.

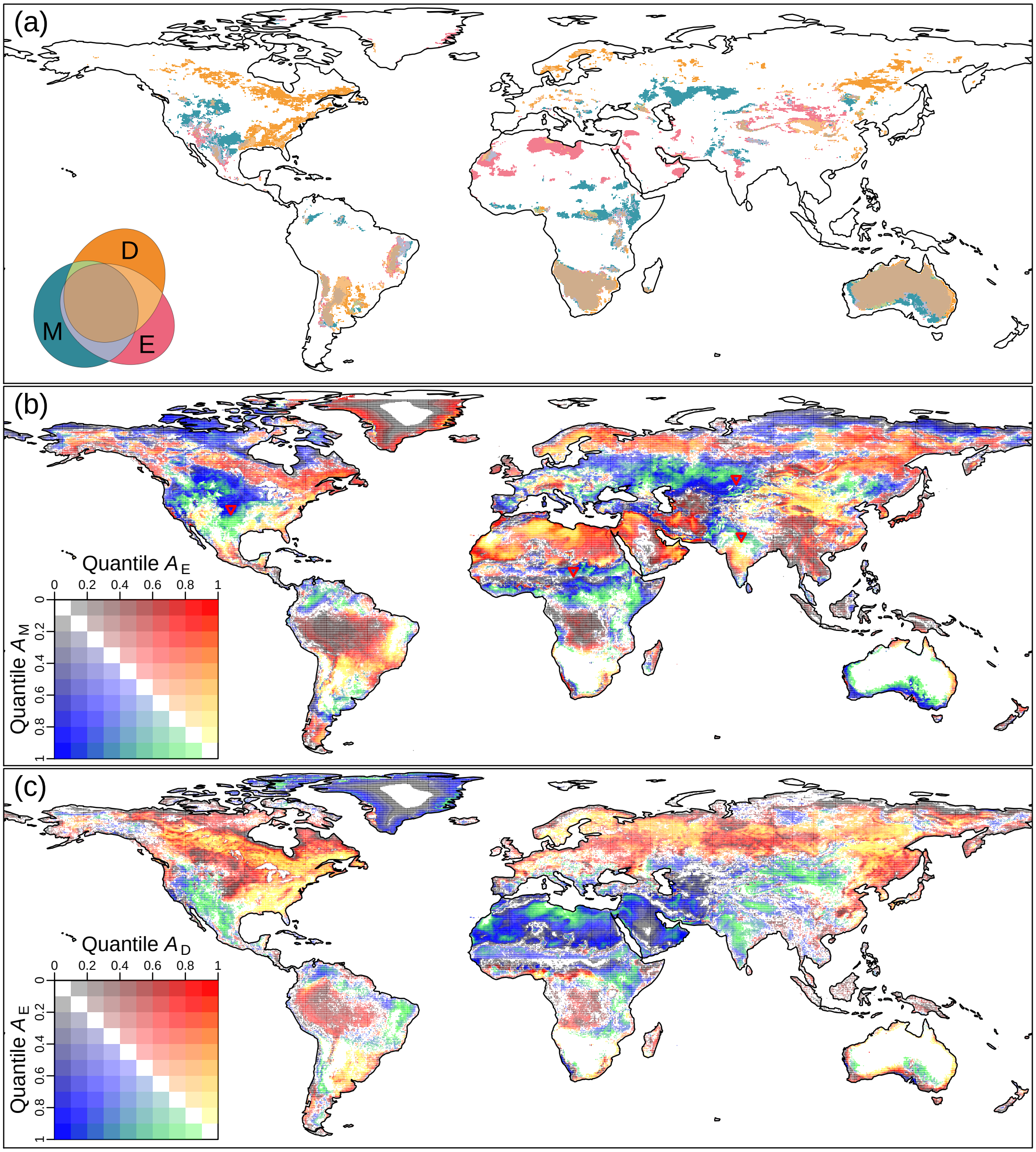

Figure 2. (a) Spatial patterns of significant $\mathcal{A}_\mathrm{M}$, $\mathcal{A}_\mathrm{E}$, and $\mathcal{A}_\mathrm{D}$ (top 10% quantile of absolute values) in summer (JJA and DJF for northern and southern hemisphere respectively). Euler diagrams show the colors for specific relationships (intersections, unions, or disjoints) among $\mathcal{A}_\mathrm{M}$, $\mathcal{A}_\mathrm{E}$, and $\mathcal{A}_\mathrm{D}$, and the areas of colored patterns also correspond to the fractions. (b)-(c) Quantile changes (b) from $\mathcal{A}_\mathrm{M}$ to $\mathcal{A}_\mathrm{E}$ and (c) from $\mathcal{A}_\mathrm{E}$ to $\mathcal{A}_\mathrm{D}$ in summer. The quantile of the $\mathcal{A}$ is separated into ten bins. The color of the grid cell is explained by the legend, where x- and y-axes indicate its quantile bins of specific $\mathcal{A}$. The diagram has three aspects of information. First, warm (cold) colors indicate quantile increase (decrease) from the original $\mathcal{A}$ (y-axis) to the final $\mathcal{A}$ (x-axis). Second, the smaller the quantile difference is, the more transparent the color. White indicates no change of quantile bin. Third, as the shifts in the large quantile bins are the main focus, we highlight this part in green and yellow. For shifts that occur within the low quantile bins, colors fade to gray. Three red triangles are samples from three regions where A is dramatically underestimated by monthly smoothing.

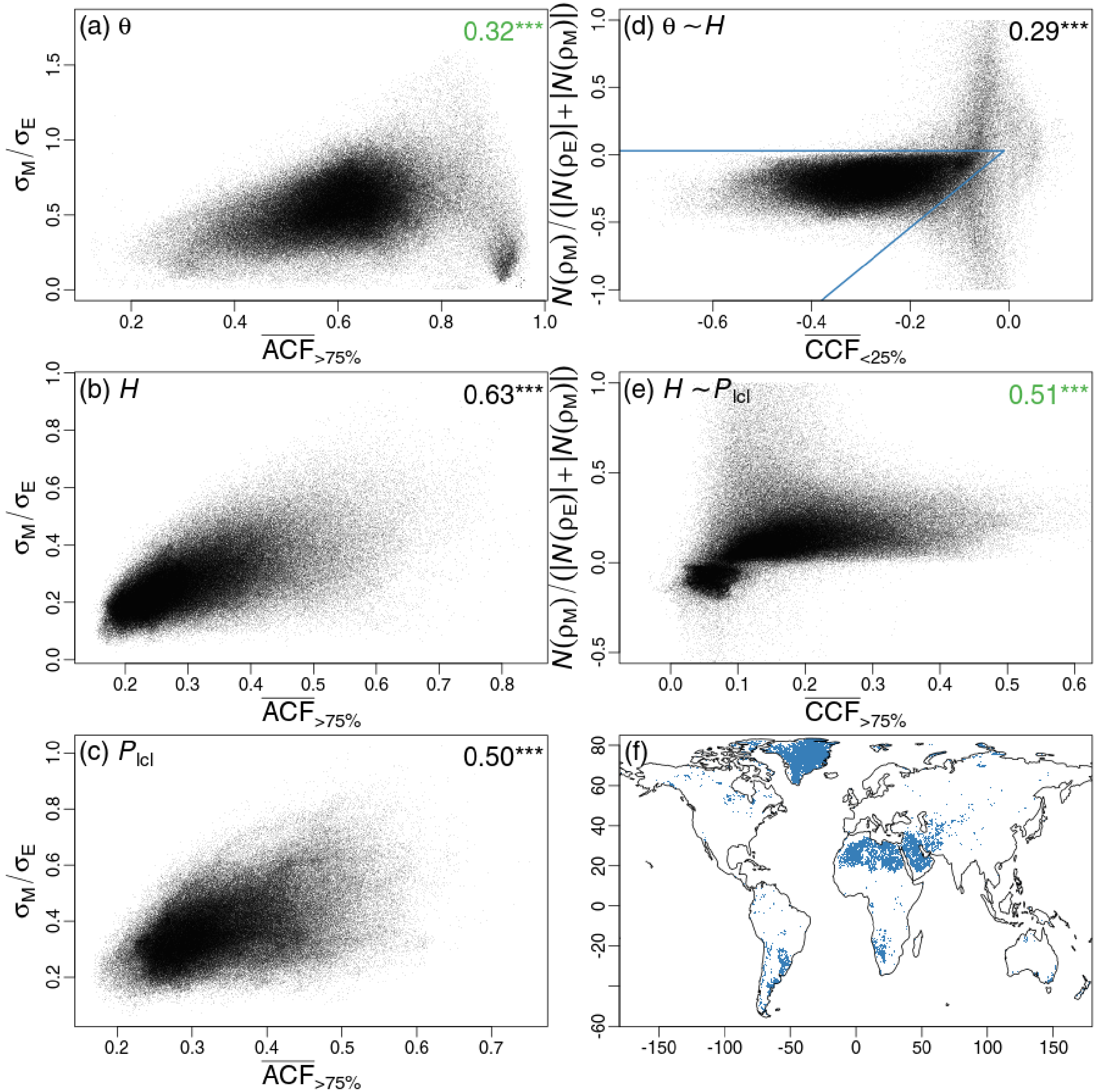

Figure 3. Scatter plot of coupling signal loss rate when moving from TLM_E to TLM_M as a function of an indicator reflecting the memory of L-A states. Points represent terrestrial grid cells around the globe. (a)–(c) Loss rate of the σ term as a function of averaged auto-correlation function ($\overline{ACF}$) with quantile larger than 75% (see Sect. 2.4). (d)–(e) Loss rate of the numerator of the ρ term (see Sect. 2.4) as a function of averaged cross-covariance function ($\overline{CCF}$) within a certain quantile range (shown by the subscript, see Sect. 2.4). Dark and green values at the top right are Person and Spearman correlation coefficients for linear and nonlinear relationships, respectively. *** indicates $p < 0.001$. (f) Patterns with values out of the main cluster (separated by two blue lines) in (e).

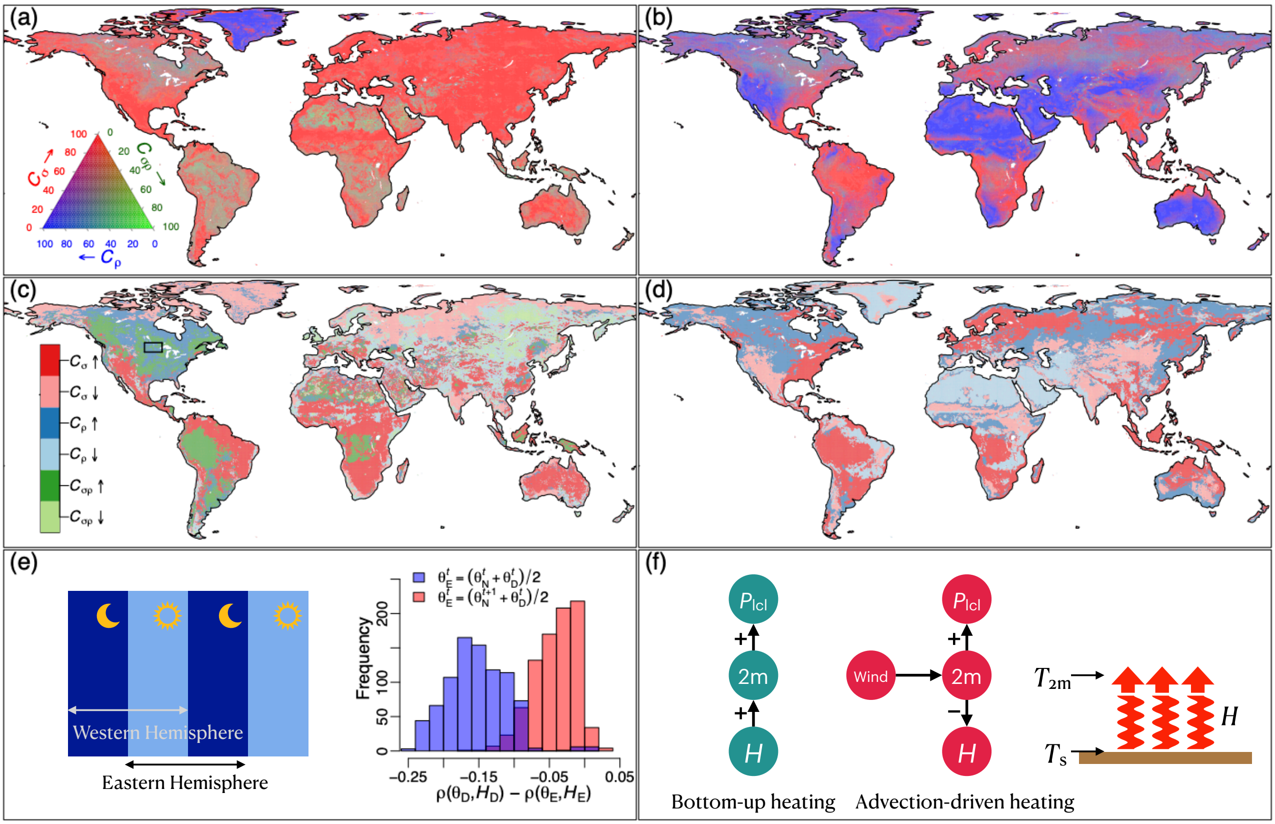

Figure 4. Comparison between $\mathrm{TLM_D}$ and $\mathrm{TLM_E}$. Left panel: the land leg ($\mathcal{L}$); right pane: the atmospheric leg ($\mathcal{A}$). Top row: fractions of the three components of $\Delta|M|$ ($|M_\mathrm{D}|-|M_\mathrm{E}|$, Eqs. 8 and 9, see Sect. 2.5). Red, blue, and green indicate contributions of fluctuation, correlation, and joint of the two ($|C_\sigma|$, $|C_\rho|$, and $|C_{\sigma\rho}|$), respectively (see Sect. 2.5). Middle row: primary contributor to pattern shift in TLM (see Sect. 2.6). The legend contains three pairs of colors: red, blue, and green indicate C_σ, C_ρ, and $C_{\sigma\rho}$ as the primary contributor, respectively. A darker (lighter) color indicates a quantile increase (decrease) from E to D. Left panel of (e): conceptual figure showing the combinations of daytime and nighttime that make up the E time series in the Eastern versus Western Hemisphere. Right panel of (e): histograms of the difference between D- and E-based $\rho(\theta, H)$. Data is from the rectangle region shown in (c). The blue histogram indicates the cases with the original θ_E (an average of the nighttime soil moisture θ_N and the following daytime soil moisture θ_D). Red histogram indicates the cases with the modified θ_E (an average of the θ_D and the following θ_N). Left and middle panel of (f): two mechanisms driving the $\mathcal{A}$. Right panel of (f): the definition of sensible heat flux H which reflects the temperature gradient from the surface to the near-surface (2m).

Supplementary information for “Daytime-only-mean data can enhance enhances understanding of land-atmosphere coupling”

Zun Yin[1], Kirsten Findell[2], Paul Dirmeyer[3], Elena Shevliakova[2], Sergey Malyshev[2], Khaled Ghannam[1], Nina Raoult[4], and Zhihong Tan[1]

[1]Program in Atmospheric and Oceanic Sciences, Princeton University, Princeton, 08540, New Jersey, USA
[2]Geophysical Fluid Dynamics Laboratory, NOAA/OAR, Princeton, 08540, New Jersey, USA
[3]Center for Ocean-Land-Atmosphere Studies, George Mason University, Fairfax, 22030, Virginia, USA
[4]Laboratoire des Sciences du Climat et de l’Environnement, IPSL, CNRS-CEA-UVSQ, Gif-sur-Yvette, 91191, Essonne, France

Correspondence: Zun Yin (zyin@princeton.edu)

This PDF file includes:

- Supplementary text 1 “The key driver of L-A coupling signal attenuation due to monthly smoothing”
- Supplementary text 2 “Atmospheric advection-dominated climate regime in Sahara”
- Figures S1 to S7

Supporting Information Text

The key driver of L-A coupling signal attenuation due to monthly smoothing

First, we introduce the algorithms of both trend and seasonal cycle removal applied to the original time series. Then, we check that the detrended-seasonal removed monthly time series is equal to the monthly mean of the detrended-seasonal removed daily time series. Finally, we separate the two-legged metrics (TLM) into the standard deviation term (σ) and the correlation coefficient term (ρ), and investigate the key factor leading to the difference between monthly- and entire-day-mean-based TLM.

Detrending and removal of the seasonal cycle. Let’s consider a daily time series x_i. To calculate the two-legged metrics, both trend and seasonality must be removed from the original values. To remove the long-term trend, we generate a linear regression model between time and the variable of interest (e.g., x_i), and then perform detrending by removing model-predicted values from original values like

$$\dot{x}_i = x_i - g(i)$$

where i is day index and $\dot{x}_i$ is detrended time series. $g(i)$ is the linear regression function retrieved from the x_i against time.

To remove the seasonal cycle, we estimate the seasonality by calculating the multi-year mean of the target value at a specific date, and then perform the removal as

$$\tilde{x}_{d,y} = \dot{x}_{d,y} - \frac{1}{Y}\sum_{i=1}^{Y}\dot{x}_{d,i}$$

where $\tilde{x}_{d,y}$ is the time series after removing the seasonality. The subscript (d,y) represents time in the form of date and year, and Y is the number of years in the averaging.

Daily and monthly time series. Here we demonstrate that detrended-seasonal removed monthly time series is equal to the monthly mean of detrended-seasonal removed daily time series. Let's assume a detrended daily time series data o_t ($t \in [1, D \times M \times Y]$). Here D, M, and Y are the numbers of day in a month, the number of months, and the number of years, respectively. The time step t can be written in the form of {day,month,year} as $t = \{d,m,y\}$ ($d \in [1,D]$, $m \in [1,M]$, $y \in [1,Y]$).Then we can get the seasonal removed daily time series O_t as

$$O_{d,m,y} = o_{d,m,y} - \frac{1}{Y}\sum_{k=1}^{Y} o_{d,m,k}$$

The detrended monthly time series p_t (t can be written as $\{m,y\}$) is

$$p_{m,y} = \frac{1}{D}\sum_{i=1}^{D} o_{i,m,y}$$

The seasonal removed monthly time series P_t is

$$\begin{aligned}
P_{m,y} &= p_{m,y} - \frac{1}{Y}\sum_{k=1}^{Y} p_{j,k} \\
&= \frac{1}{D}\sum_{i=1}^{D} o_{i,m,y} - \frac{1}{Y}\sum_{k=1}^{Y} p_{m,k} \\
&= \frac{1}{D}\left(\sum_{i=1}^{D} o_{i,m,y} - \frac{1}{Y}\sum_{i=1}^{D}\sum_{k=1}^{Y} o_{i,m,k}\right) \\
&= \frac{1}{D}\sum_{i=1}^{D}\left(o_{i,m,y} - \frac{1}{Y}\sum_{k=1}^{Y} o_{i,m,k}\right) \\
&= \frac{1}{D}\sum_{i=1}^{D} O_{i,m,y}
\end{aligned}$$

Differences between M- and E-based TLMs. First, let's have a look at the σ term of the TLMs. To keep the symbols simple, we denote a_i and b_i (i is day index) as detrended and seasonal removed daily time series. A_j and B_j (j is the month index) are corresponding monthly time series. As the long-term average of b_i (i.e., $\bar{b}$) is zero, the σ_b can be expressed as

$$\sigma_b = \left(\frac{1}{DMY}\sum_{i=1}^{DMY} b_i^2 - \bar{b}^2\right)^{\frac{1}{2}}$$
$$= \left(\frac{1}{MY}\sum_{i=1}^{MY}\left(\frac{b_i^2 + b_{i+1}^2 + b_{i+2}^2 + ... + b_{i+D}^2}{D}\right)_j\right)^{\frac{1}{2}}$$

D, M, and Y are the number of days, months, and years, respectively. The σ_B can be written as

$$\sigma_{B_j} = \left(\frac{1}{MY}\sum_{j=1}^{MY} B_j^2 - \bar{B}^2\right)^{\frac{1}{2}}$$
$$= \left(\frac{1}{MY}\sum_{j=1}^{MY}\left(\frac{\sum_{i\in j}^{D} b_i}{D}\right)^2\right)^{\frac{1}{2}}$$
$$= \left(\frac{1}{MY}\sum_{j=1}^{MY}\left[\frac{(b_i + b_{i+1} + b_{i+2} + ... + b_{i+D})^2}{D^2}\right]_j\right)^{\frac{1}{2}}$$

The difference between σ_b and σ_B is illustrated in Fig. ??. σ_b contains all squared b_i (dark boxes in Fig. ??), but σ_B contains averaged products of all combinations of b_i within a month.

It is not difficult to proof that $D^2\sum_{i=1}^{N} b_i^2 \geq (b_i + b_{i+1} + ... + b_N)^2$. The equal relation stands when $b_i = b_{i+1} = ... = b_N$, indicating all daily variables are the same within a month. Considering all months, the σ_B is larger if b_i follows the Matthew principle better, that is large values assemble together in specific months and small values assemble together in other months. As b_i is a time series of variables in a natural process. b_i is somehow correlated with itself at a certain time scale, that is the memory of b_i. It implies that if b_i is large, its neighbours (e.g., b_{i-1} and b_{i+1}) are large as well. Thus, the memory (characterized by auto-correlation) may determine the information loss from σ_b to σ_B, if the σ_b is considered as the accurate information we want.

The ρ term based on daily time series can be written as:

$$\rho(a,b) = \frac{\sum_{i=1}^{DMY}(a_i - \bar{a})\left(b_i - \bar{b}\right)}{\sigma_a\sigma_b}$$
$$= \frac{\sum_{i=1}^{DMY} a_i b_i}{\sigma_a\sigma_b}.$$

$\bar{a}$ and $\bar{b}$ are mean of a_i and b_i, respectively. Similarly, we can get $\rho(A,B)$ as

$$\rho(A,B) = \frac{\sum_{j=1}^{MY}\left(A_j - \bar{A}\right)\left(B_j - \bar{B}\right)}{\sigma_A \cdot \sigma_B}$$
$$= \frac{1}{\sigma_A\sigma_B}\sum_{j=1}^{MY}\left(\frac{\left(\sum_{i\in j} a_i\right)\left(\sum_{i\in j} b_i\right)}{D^2}\right).$$

The ρ term contains σ terms, which has been discussed in the previous section. If we focus on the numerator, we can find that the difference of numerator between E and M has a similar structure as the ρ difference between E and M. Thus, we deduct that the cross-covariance between a_i and b_i is the key contributor to the difference of the ρ's numerator between E and M.

Atmosphric Atmospheric advection-dominated climate regime in Sahara

Unlike most other places, the atmospheric leg ($\mathcal{A}$) across the Sahara region is negative (Fig. S5), suggesting a negative correlation between the sensible heat flux (H) and the pressure at the LCL (P_{lcl}). This atypical signal is present presents in all seasons and may be caused by a special mechanism driven by atmospheric advection. Northerly winds from the Mediterranean Sea cool and moisten the near-surface air of the Sahara region, while southerly winds warm and dry the surface (Fig. S6a). According to ERA5, the correlation between E-based daily northward wind speed ($v_{10\mathrm{m}}$) and the 2-m air temperature ($T_{2\mathrm{m}}$) for ten-year JJA data at a sample grid cell in the Sahara is 0.63 (Fig. S6b), which is much larger than that of the eastward wind case (0.12, not shown). On the other hand, the northerly winds show a high correlation with the 2-m absolute humidity (AH), as well (-0.67, Fig. S6b). This suggests that atmospheric advection may determine the inter-daily fluctuations of near-surface temperature and humidity rather than the sensible heat flux from the surface. One piece of evidence is that $T_{2\mathrm{m}}$ fluctuates synchronously with H in the Sahara, with Fig. S6c showing that the auto-correlation is strongest with no time lag between variables. If the $T_{2\mathrm{m}}$ is driven by the surface through H then the peak correlation should occur with a few hours time lag between H and $T_{2\mathrm{m}}$, as shown for an example European grid cell in Fig. S6d.

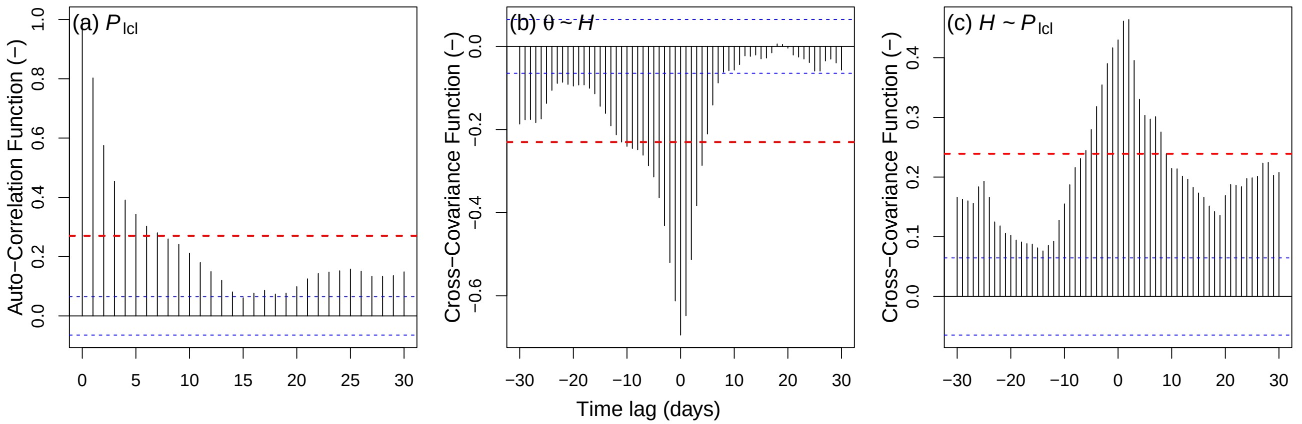

Figure S1. Illustration Examples of calculating memory indicator for the difference between σ_b σ term and σ_B for the numerator of the ρ term ($N(\rho)$) of the two-legged metrics. Small boxes indicate daily time series (a) The entire-day-mean-based $\sigma_{P_{\mathrm{lcl}}}$ for instance, at one grid cell we first calculate the auto-correlation function (ACF) of b_i P_{lcl} with the maximum lag of 30 days. And large boxes Then the top 25% quantile of these correlation coefficients are selected (red dashed lines indicate monthly time series B_j the threshold) and averaged as the indicator $\overline{\mathrm{ACF}}_{\geqslant 75\%}$. For month j (i.e., top middle box b) For the paired θ and H, dark small boxes indicate components we calculate the cross-covariance function (CCF) with the maximum lag of σ_b $\pm$30 days. As the $\rho(\theta, H)$ is negative, we select the lowest 25% correlation coefficients and calculated the mean (Eq $\overline{\mathrm{CCF}}_{<25\%}$) as indicator. ??(c) Similar to (b), but selecting the top 25% correlation coefficients to calculate the indicator.

Maps of normalized two-legged metrics (TLMs) in JJA. Top to bottom panel: land, atmospheric, and total leg. Left to right panel: monthly-, entire-day-mean-, and daytime-only-based TLMs. To make the $\mathrm{TLM_M}$, $\mathrm{TLM_E}$ and $\mathrm{TLM_D}$ comparable, we normalize specific TLM by $n_i = \min(\max(x_i/q_{99.9\%}, -1), 1)$, where n_i indicates the normalized value of x_i and the $q_{99.9\%}$ is the 99.9% quantile of $|x_i|$. Gray regions indicate associated correlation is not significant ($p > 0.05$)

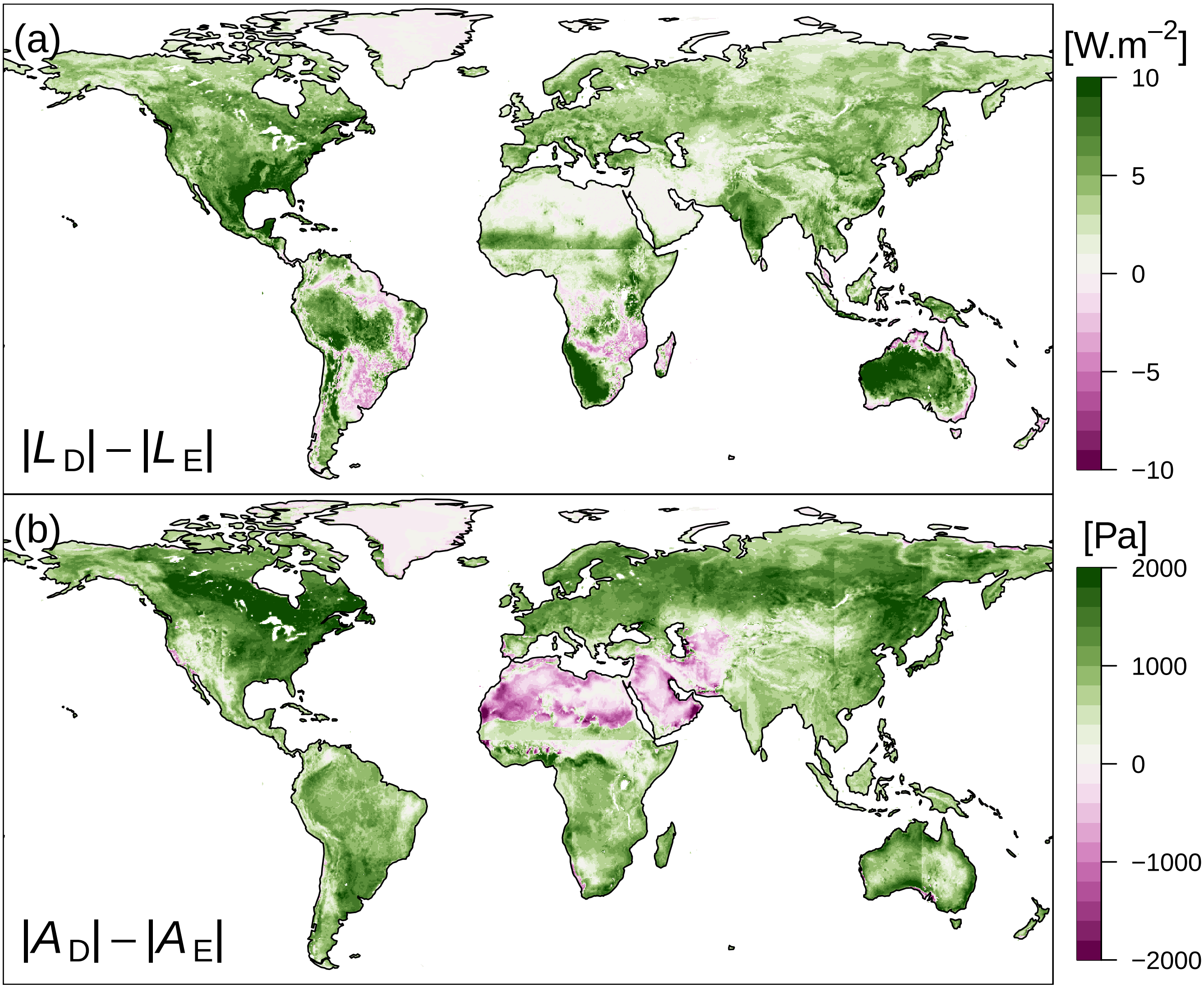

Figure S2. (a) Difference between $|\mathcal{L}_D|$ and $|\mathcal{L}_E|$ in summer (JJA and DJF for the Northern and Southern Hemisphere, respectively). (b) Same as (a) but for the atmospheric leg ($\mathcal{A}$).

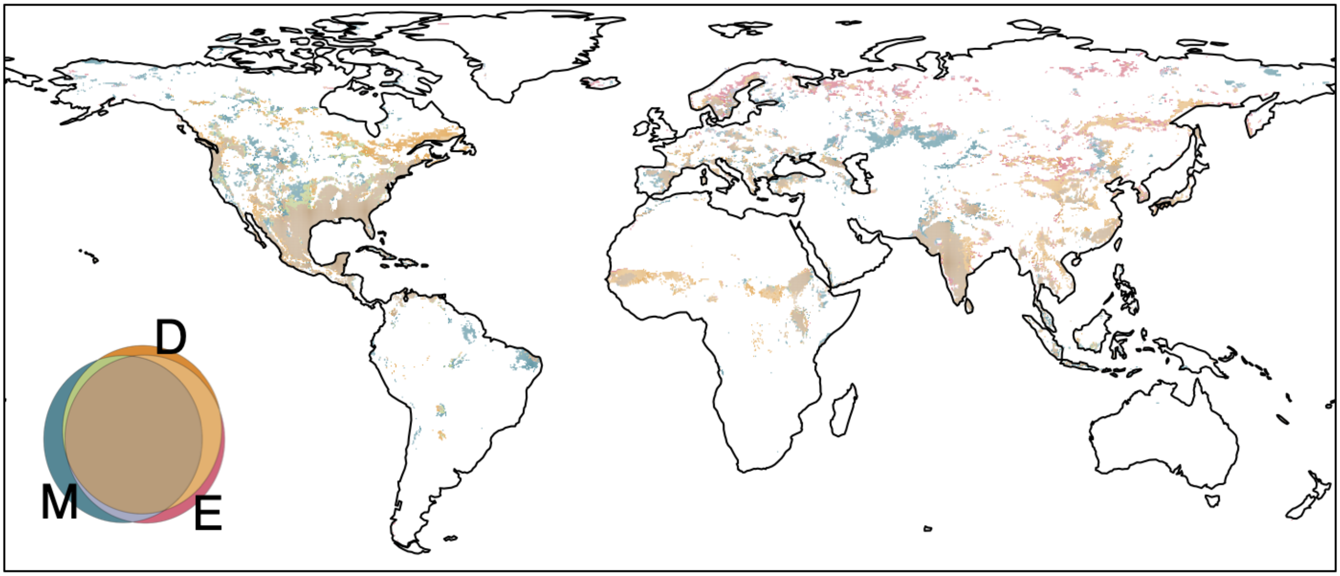

Figure S3. Spatial patterns of significant $\mathcal{L}_{\mathrm{M}}$, $\mathcal{L}_{\mathrm{E}}$, and $\mathcal{L}_{\mathrm{D}}$ (top 90% quantile of absolute values) in summer (JJA and DJF in the Northern and Southern Hemisphere, respectively). Euler diagrams show the colors for specific relationships (intersections, unions, or disjoints) among $\mathcal{L}_{\mathrm{M}}$, $\mathcal{L}_{\mathrm{E}}$, and $\mathcal{L}_{\mathrm{D}}$, and the areas of colored patterns indicate the fractions of them as well.

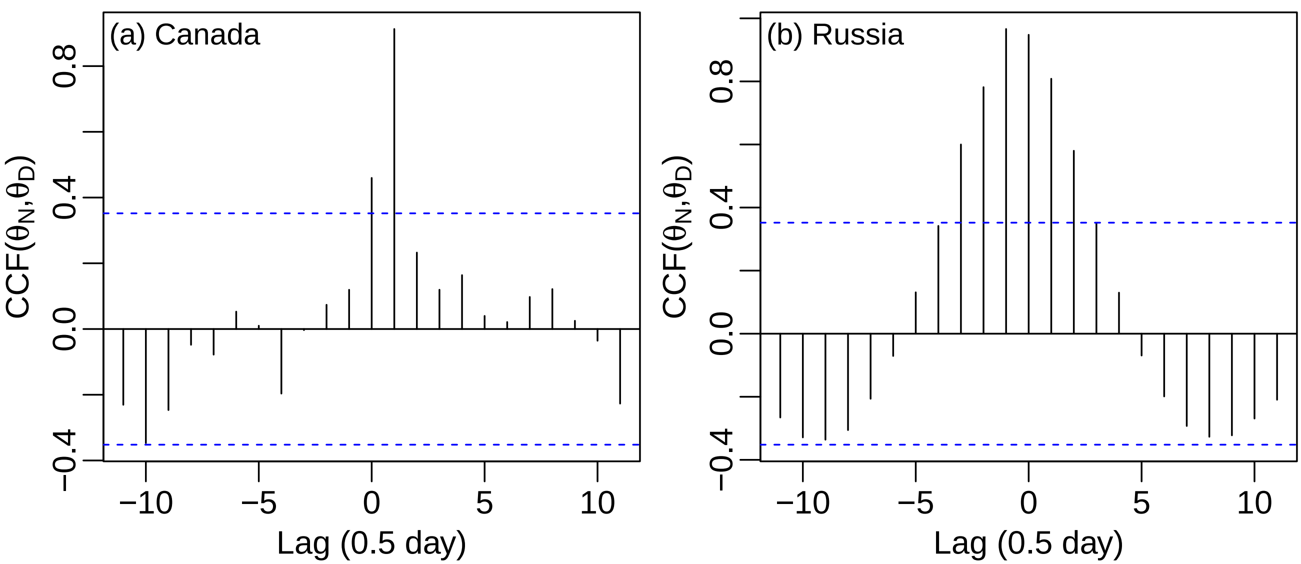

Figure S4. (a) ~~Cross correlation~~ Cross-correlation function between nighttime-only-mean (N) and daytime-only-mean (D) soil moisture (θ_{N} and θ_{D}) in a grid cell located in Canada ([82.25°W, 47.5°N]). (b) Same as (a), but the grid cell is taken as a reference in Russia ([122.5°E, 68.5°N]).

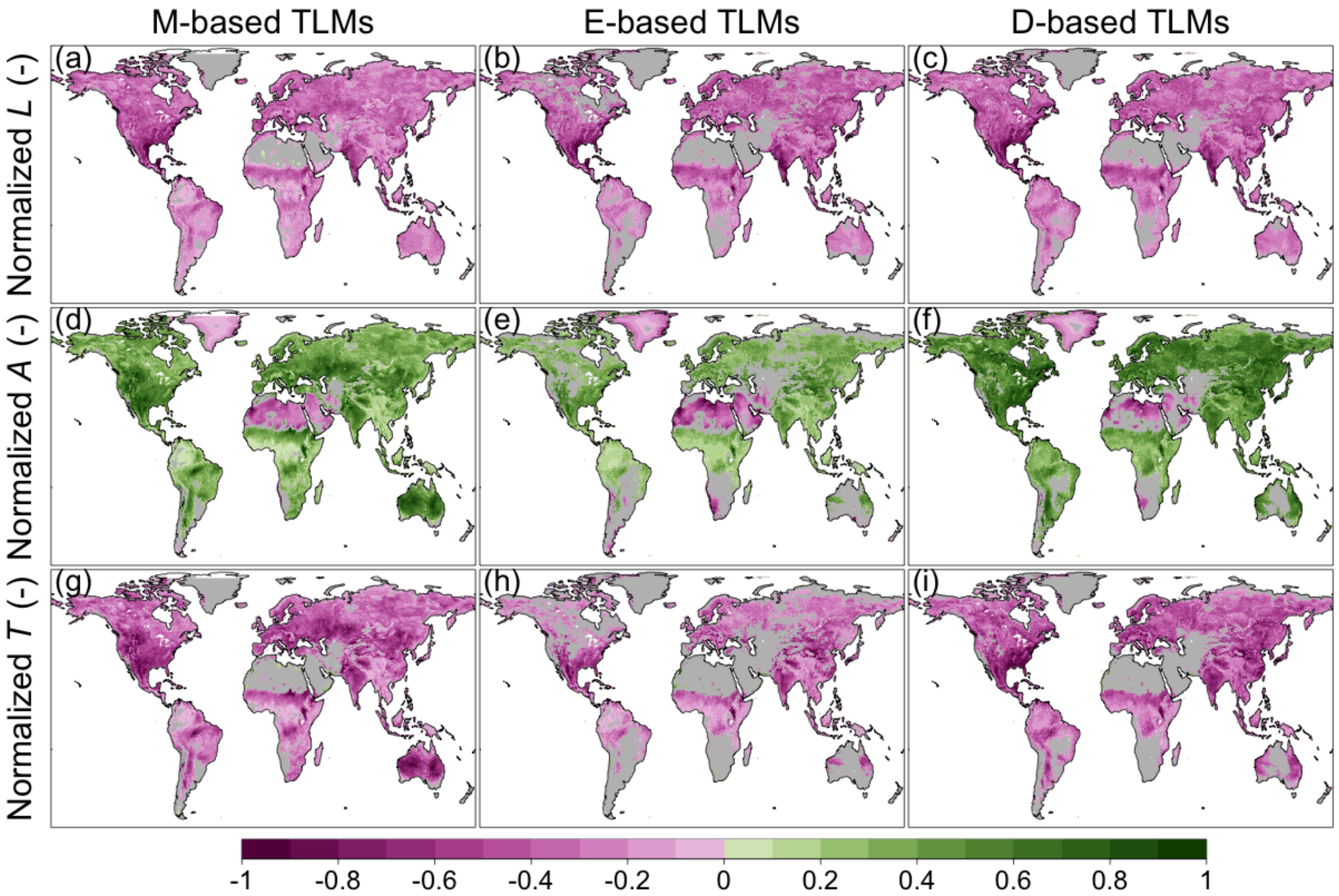

Figure S5. Maps of normalized two-legged metrics (TLMs) in JJA. Top to bottom panel: land, atmospheric, and total leg. Left to right panel: monthly-, entire-day-mean-, and daytime-only-based TLMs. To make the TLM_M, TLM_E and TLM_D comparable, we normalize specific TLM by $n_i = \min(\max(x_i/q_{99.9\%}, -1), 1)$, where n_i indicates the normalized value of x_i and the $q_{99.9\%}$ is the 99.9% quantile of $|x_i|$. Gray regions indicate associated correlation is not significant ($p \geq 0.05$)

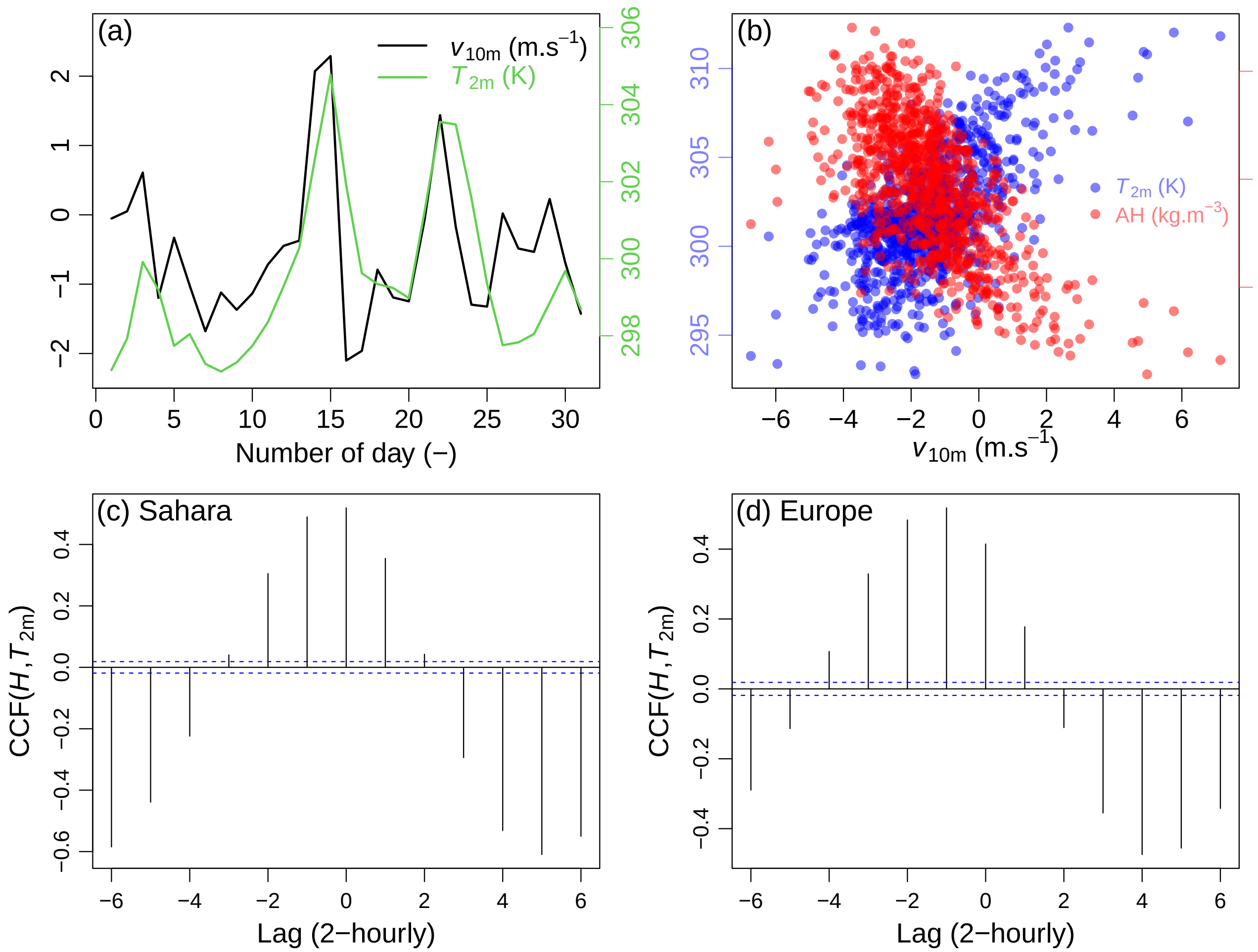

Figure S6. An example of atmospheric advection driven L-A interaction mechanism. (a) Daily 10-m northward wind speed ($v_{10\mathrm{m}}$) and $T_{2\mathrm{m}}$ for the entire day in July 2015. (b) $T_{2\mathrm{m}}$ and 2m absolute humidity (AH) as a function of $v_{10\mathrm{m}}$. The illustration is based on entire-day-mean daily values in JJA from 2011 to 2020. (c)–(d) Cross-covariance between two-hourly H (positive up) and $T_{2\mathrm{m}}$ based on two grid cells in Sahara ([12°E, 32.75°N]) and in Europe ([12°E, 47.75°N]), respectively. y-axis indicates the correlation coefficients between $T_{2\mathrm{m}}$ and a time-shifted H time series. The x-axis indicates the time steps of the H shifted. Negative (positive) values indicate lagged (ahead).

~~Examples of calculating memory indicator for the σ term and for the numerator of the ρ term ($N(\rho)$) of the two-legged metrics. (a) The entire-day-mean-based $\sigma_{P_{\mathrm{lcl}}}$ for instance, at one grid cell we first calculate the auto-correlation function (ACF) of P_{lcl} with the maximum lag of 30 days. Then the top 25% quantile of these correlation coefficients are selected (red dashed lines indicate the threshold) and averaged as the indicator $\overline{\mathrm{ACF}}_{>75\%}$. (b) For the paired θ and H, we calculate the cross-covariance function (CCF) with the maximum lag of ±30 days. As the $\rho(\theta, H)$ is negative, we select the lowest 25% correlation coefficients and calculated the mean ($\overline{\mathrm{CCF}}_{<25\%}$) as indicator. (c) Similar to (b), but selecting the top 25% correlation coefficients to calculate the indicator.~~